Title

NaV1.1 channels in axon initial segments of bipolar cells augment input to magnocellular visual pathways in the primate retina.

Journal

Journal of Neuroscience, 33(41)

Authors

Venkataramani, Sowmya
Gayet-Primo, Jacqueline
Smith, Robert
et al.

Publication Date

2013-10-09

DOI

10.1523/JNEUROSCI.1249-13.2013

Peer reviewed

Systems/Circuits

$Na_V1.1$ Channels in Axon Initial Segments of Bipolar Cells Augment Input to Magnocellular Visual Pathways in the Primate Retina

Theresa Puthussery,[1] Sowmya Venkataramani,[1] Jacqueline Gayet-Primo,[1] Robert G. Smith,[2] and W. Rowland Taylor[1]

[1]Casey Eye Institute, Department of Ophthalmology, Oregon Health & Science University, Portland, Oregon 97239, and [2]Department of Neuroscience, University of Pennsylvania, Philadelphia, Pennsylvania 19104

In the primate visual system, the ganglion cells of the magnocellular pathway underlie motion and flicker detection and are relatively transient, while the more sustained ganglion cells of the parvocellular pathway have comparatively lower temporal resolution, but encode higher spatial frequencies. Although it is presumed that functional differences in bipolar cells contribute to the tuning of the two pathways, the properties of the relevant bipolar cells have not yet been examined in detail. Here, by making patch-clamp recordings in acute slices of macaque retina, we show that the bipolar cells within the magnocellular pathway, but not the parvocellular pathway, exhibit voltage-gated sodium (Na_V), T-type calcium (Ca_V), and hyperpolarization-activated, cyclic nucleotide-gated (HCN) currents, and can generate action potentials. Using immunohistochemistry in macaque and human retinae, we show that $Na_V1.1$ is concentrated in an axon initial segment (AIS)-like region of magnocellular pathway bipolar cells, a specialization not seen in transient bipolar cells of other vertebrates. In contrast, $Ca_V3.1$ channels were localized to the somatodendritic compartment and proximal axon, but were excluded from the AIS, while HCN1 channels were concentrated in the axon terminal boutons. Simulations using a compartmental model reproduced physiological results and indicate that magnocellular pathway bipolar cells initiate spikes in the AIS. Finally, we demonstrate that Na_V channels in bipolar cells augment excitatory input to parasol ganglion cells of the magnocellular pathway. Overall, the results demonstrate that selective expression of voltage-gated channels contributes to the establishment of parallel processing in the major visual pathways of the primate retina.

Introduction

A central goal for understanding visual function is to determine how parallel retinal circuits produce the characteristic outputs of different retinal ganglion cell types. In primates, the midget and parasol ganglion cells are the most abundant and well characterized retinal output neurons, providing the neural substrate for the parvocellular and magnocellular visual pathways, respectively (Perry et al., 1984; Watanabe and Rodieck, 1989). Parasol ganglion cells exhibit transient light responses and respond to high-temporal frequency stimuli, making them fundamental for the perception of motion and flicker. On the other hand, midget ganglion cells exhibit relatively sustained light responses, and show comparatively low temporal resolution, but are optimized for form and color vision (De Monasterio and Gouras, 1975; for review, see Dacey, 2004; Lee et al., 2010). The neural mechanisms that underlie the differential tuning of parasol and midget ganglion cells are not well understood, but the differences are presumed to arise at the level of the bipolar cells (for review, see Masland, 2012).

There are at least 10 morphologically distinct cone bipolar cell types in the macaque and human retina (Boycott and Wässle, 1991; Haverkamp et al., 2003); these can be divided into OFF and ON types, which respond to decrements and increments in light intensity. The flat midget bipolar (FMB) and invaginating midget bipolar (IMB) cells provide input to the OFF and ON midget ganglion cells, respectively (Polyak, 1941; Kolb and Dekorver, 1991; Calkins et al., 1994), whereas the diffuse bipolar (DB) cell type DB3 provides the major input to OFF parasol ganglion cells (Jacoby et al., 2000; Calkins and Sterling, 2007), and DB4 cells likely provide input to ON parasol cells (Boycott and Wassle, 1991). The functional properties of these bipolar cells have not been examined in detail, but work in other mammals suggests that functional diversity could arise, as follows: (1) at the dendritic input, through differences in glutamate receptors (Awatramani and Slaughter, 2000; DeVries, 2000); (2) at the axon terminal output, through differences in calcium dynamics (Baden et al., 2013a) and amacrine cell connectivity (Eggers and

Received March 22, 2013; revised Aug. 20, 2013; accepted Aug. 24, 2013.

Author contributions: T.P. and W.R.T. designed research; T.P., S.V., and J.G.-P. performed research; R.G.S. contributed unpublished reagents/analytic tools; T.P., S.V., R.G.S., and W.R.T. analyzed data; T.P. and W.R.T. wrote the paper.

This research was supported by National Eye Institute Grants EY014888 (W.R.T.) and EY016607 (R.G.S.); a Research to Prevent Blindness (RPB) Lew R. Wasserman Merit Award (W.R.T.); a Collins Medical Trust Grant (T.P.); an unrestricted RPB grant to the Department of Ophthalmology, Oregon Health & Science University (OHSU), and the Ophthalmology (P30-EY010572) and Advanced Imaging core (P30-NS061800) facilities at OHSU. We thank Dr. Francoise Haeseleer for providing the CaBP5 antibody; Drs. Paul Martin, Ulrike Grünert, and Ilya Buldyrev for comments on earlier versions of the manuscript; and Drs. David Wilson and Alison Skalet for providing human tissue samples.

The authors declare no competing financial interests.

Correspondence should be addressed to W. Rowland Taylor, Department of Ophthalmology, Oregon Health & Science University, 3375 SW Terwilliger Boulevard, Portland, OR 97239. E-mail: taylorw@ohsu.edu.

DOI:10.1523/JNEUROSCI.1249-13.2013

 0270-6474/13/3316045-15$15.00/0

Lukasiewicz, 2011); and (3) intrinsically, through differences in expression of voltage-gated channels (Ma et al., 2003; Müller et al., 2003; Cui and Pan, 2008). Here, we exploit the well characterized circuits of the macaque retina to determine how voltage-gated channels in bipolar cells contribute to the physiological properties of the major ganglion cell types.

There is mounting evidence that not all bipolar cells signal exclusively through graded voltage signals; some exhibit voltage-gated sodium (Na_V) and calcium (Ca_V) currents and can produce spikes (Cui and Pan, 2008; Saszik and DeVries, 2012; Baden et al., 2013a,b). Such bipolar cells have not been identified in primate retina (Han et al., 2000), and it is not clear in any species which channel subunits drive spiking, where the channels are located, whether the channels are functionally significant, or which retinal circuits these bipolar cells are part of. Here, we provide evidence that voltage-gated channels in bipolar cells contribute to functional differences in the magnocellular and parvocellular visual pathways.

Materials and Methods

Tissue preparation. Eyes were obtained from adult rhesus (*Macaca mulatta*) or cynomolgus macaques (*Macaca fascicularis*) of either sex. The tissue was recovered immediately postmortem from animals that were exsanguinated in the course of unrelated experiments at the Oregon National Primate Research Center (ONPRC). All animal procedures were performed in accordance with the ONPRC Tissue Distribution Program. The anterior eye and vitreous were removed under room lighting, and the posterior eyecups maintained in bicarbonate-buffered Ames medium (US Biologicals) equilibrated with 95% O_2/5% CO_2, pH 7.4, for ~30 min. After this time, the retina/retinal pigment epithelium/choroid were removed from the sclera, and stored in the same buffer at 25°C until further use. A sample of peripheral adult human retina was obtained from an eye that had been enucleated for the management of an extensive choroidal melanoma. Tissue use was reviewed by the Oregon Health & Science University Institutional Review Board and deemed to be nonhuman subject research. Some evidence of prior serous retinal detachment was evident in the tissue sample with some degeneration of photoreceptor outer segments. The overall pattern of ion channel expression was similar to that obtained in the macaque retina, and thus it is unlikely that the loss of photoreceptor integrity substantially altered the immunostaining patterns.

Antibodies and cell markers. DB3a cells (formerly DB3) of humans and macaques were immunolabeled with a rabbit anti-calbindin (CalB) antibody (1:8000; catalog #CB38, Swant). Human DB3b cells were labeled with a mouse anti-CD15 antibody (conjugated to FITC; catalog #347423, BD Biosciences). DB4 cells of humans and macaques were labeled with a rabbit anti-protein kinase C alpha (PKCα) antibody (1:40,000; catalog #P4334, Sigma). Note that, although PKCα also labels rod bipolar cells, DB4 cells can be readily discriminated by their smaller somata, thinner axons, distinct axon terminal stratification [stratum 3 (S3)], and lower level of PKCα immunoreactivity. DB3a and DB3b cells were identified with rabbit anti-calcium binding protein 5 (CaBP5) antibody (1:500; gift from Dr. F. Haeseleer, University of Washington, Seattle, WA). This antibody also labels DB4 and rod bipolar cells. These primate bipolar cell markers have been characterized previously (Grünert et al., 1994; Haverkamp et al., 2003), and a summary of the distributions of these markers is provided in Figure 13. Mouse monoclonal antibodies for $Na_V1.1$ (1:100–1:1000; Clone K74/71, catalog #75–023), $Ca_V3.1$ (1:8; Clone N178A/9, catalog #73–206, tissue culture supernatant), hyperpolarization-activated, cyclic nucleotide-gated (HCN) channel 1 (1:1000; Clone N70/28, catalog #75–110), fibroblast growth factor (FGF)-14 (1:1000; Clone N56/21, catalog #75–096), and Ankyrin G (AnkG; 1:3000; Clone N106/36 catalog #75–187) were all obtained from the University of California, Davis (UC Davis)/NIH NeuroMab Facility. A goat anti-Ankyrin G antibody (1:1000; sc-31778, Santa Cruz Biotechnology) was also used—this antibody produced an identical pattern of staining as the monoclonal Ankyrin G antibody from the UC Davis/NIH NeuroMab Facility.

Immunohistochemistry. For immunohistochemistry on sections, pieces of peripheral retina (>4 mm) were fixed in 4% paraformaldehyde (PFA) at 25°C from 5 to 30 min. Short fixation times (5 min) were critical to preserve the antigenicity of the $Na_V1.1$ subunit. After fixation, retinae were cryoprotected in sucrose solutions (10%, 20%, and 30%), embedded in cryosectioning medium, and cut transversely at 14 μm on a cryostat. Cryostat sections were blocked for 1 h in an incubation buffer (IB) containing 3% normal horse serum, 0.3–1% Triton X-100 (TX-100), and 0.025% NaN_3. Primary antibodies were diluted in IB and applied overnight at 25°C or 4°C. Secondary antibodies, raised in donkey, and coupled to Alexa Fluor 488, 594, and/or 647 (Invitrogen), were diluted in IB without TX-100 (1:800) and applied for 1 h at 25°C. Confocal imaging was performed on an Olympus FV1000 confocal microscope with an Olympus Plan Apo (60×/1.42 oil) objective at a resolution of 7.7 pixels/μm. Image channels were pseudo-colored into RGB (red, green, blue) color space using Adobe Photoshop CS. In some cases, linear alterations to image contrast were made to the entire image using Adobe Photoshop CS.

Immunohistochemistry and imaging after patch-clamp recordings. Bipolar and ganglion cells were anatomically classified by visual inspection of the fluorescence fill at the conclusion of the recordings. In some cases, the patch pipette was removed, and the vibratome slice or whole mount was fixed in 4% PFA for 15–30 min and imaged on a confocal microscope (Figs. 1*A–C*, 3*A*,*B*). For immunohistochemistry, slices and whole mounts were incubated in IB for 5–7 d at 25°C. Secondary antibodies were diluted in IB without TX-100 (1:800) and applied overnight at 25°C. For illustration of bipolar cell morphology (Fig. 1*A*), confocal *z*-stacks were combined into a single image plane and overlayed on a transmitted light view from a confocal plane focused at the level of the axon terminals. The "despeckle" tool in ImageJ was sometimes used to uniformly remove noisy pixels from these image stacks.

To obtain comparative intensity profiles of HCN1 and ON parasol dendrites, whole mounts in which ON parasol cells were filled were processed for immunolabeling with HCN1. Z-stacks were acquired to span the entire depth of the inner plexiform layer (IPL). Average intensity profiles were measured for each color channel at each *z*-position of the IPL and were obtained from three regions of interest (10 × 10 μm) for each cell. The *z*-resolution was 0.89 μm. IPL depth was calibrated from vertical sections stained for HCN1.

Axon initial segment position analysis. The intensity of immunostaining for axon initial segment (AIS)-associated proteins and ion channels in bipolar cell axonal profiles was measured from confocal *z*-stacks of cryostat sections that were maximally projected onto a single image plane. Optical sections were 0.897 μm thick, taken at *z*-intervals of 0.44 μm. The *x*,*y* resolution was 4.6 pixels/μm. RGB intensity measurements were made from a line, 4 pixels wide, traced along the axon from the base of the soma to the axon terminals. Intensity values were normalized to the maximum intensity within each color channel. To compare the location of $Ca_V3.1$ and AnkG in Figure 7*G*, profiles from 23 DB4 cells, taken from three retinae were averaged together. Before averaging, the profiles were aligned to the start position of the AIS, as evident from the AnkG staining. The start position of the AnkG staining was defined as the point at which the fluorescence had increased to 50% of maximum. Intensities are reported as the mean ± SEM. To determine the absolute stratification level of $Na_V1.1$ immunostaining relative to retinal depth (see Fig. 5*L*), intensity profiles spanning from outer plexiform layer (OPL) to IPL were generated from transverse sections of retina. For each region of interest, a confocal stack spanning a *z*-distance of 3.2 μm was acquired and projected onto a single image plane. Analysis was performed over a total retinal length of 2647 μm (n = 3 animals). The inner nuclear layer (INL)/IPL border was registered in each image and used as a reference to vertically align the images. The vertical scaling of each image was set to equalize the distance from the OPL to the inner border of the IPL.

Bipolar cell recordings. For macaque bipolar cell recordings, the pigment epithelium/choroid was removed and the isolated retina (eccentricity, ~4–8 mm) was embedded in 3% low-melting point agarose (Lonza) dissolved in HEPES-buffered Ames medium, and sectioned at

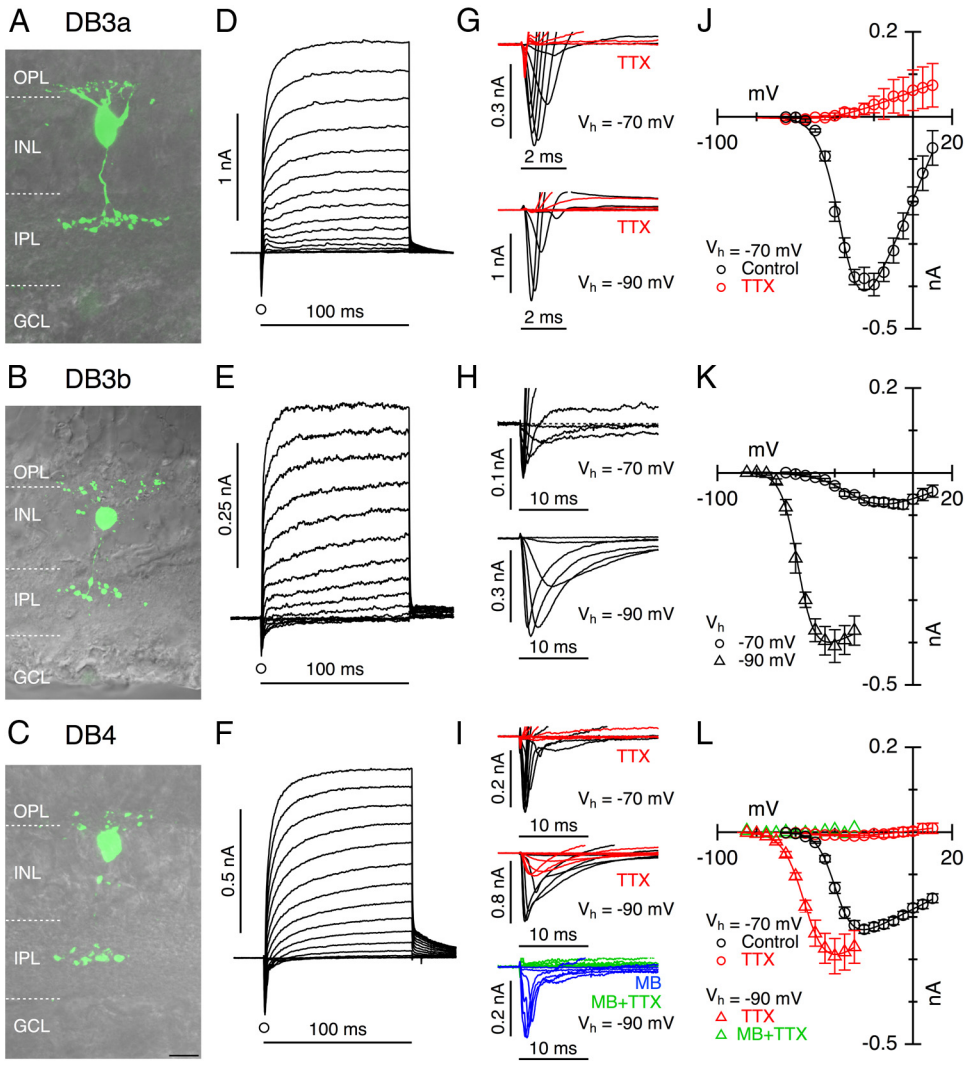

Figure 1. Bipolar cells of the magnocellular pathway exhibit large Na_v currents and T-type Ca_v currents. ***A–C***, Confocal projections showing examples of DB3a (***A***), DB3b (***B***), and DB4 (***C***) cells overlayed on a transmitted light image of the same field. Retinal layers are indicated to the left of the panels. ***D–F***, Leak-subtracted currents activated by 100 ms long depolarizing voltage steps from −65 to +15 mV in 5 mV increments. $V_h = -70$ mV. Traces are averages from $n = 20$ (DB3a; ***D***), $n = 13$ (DB3b; ***E***), and $n = 34$ (DB4; ***F***). The round symbols show the time points used for the *I–V* relations in the right-hand panels (***J–L***). Note the presence of inward currents at the start of the voltage steps. ***G***, Top, Data from ***D*** showing the inward currents on an expanded timescale (black traces). These currents were completely blocked by application of the Na_v channel blocker, TTX (red traces, $n = 4$). Bottom, $V_h = -90$ mV; average currents activated by voltage steps from −80 mV to −30 mV in 10 mV increments (black traces, $n = 10$). The inward currents are completely blocked by application of TTX (red traces, $n = 2$). ***H***, Top, Data from ***E*** showing inward currents on an expanded timescale. Bottom, $V_h = -90$ mV; average inward currents activated by voltage steps from −80 mV to −30 mV in 10 mV increments ($n = 10$). ***I***, Top, Data from ***F*** showing control inward currents on an expanded timescale (black traces). Inward currents are completely blocked by application of TTX (red traces, $n = 8$). Middle and bottom, $V_h = -90$ mV; average currents activated by voltage steps from −80 to −30 mV in 10 mV increments in control (middle, black, $n = 8$), 0.5 μM TTX (middle, red, $n = 5$), mibefradil (MB, bottom, blue, $n = 3$), or mibefradil plus TTX (bottom, green, $n = 2$). Note that the TTX-resistant inward current is blocked with the T-type Ca_v channel blocker mibefradil. ***J–L***, Maximum inward current amplitudes (±SEM) near the onset of the voltage steps for DB3a (***J***), DB3b (***K***), and DB4 (***L***) cells. The red data points in ***J*** and ***L*** were recorded in TTX. The green data points in ***L*** were recorded in the presence of mibefradil plus TTX. The smooth lines through the data points fit to a Boltzmann activation function. The triangles in ***K*** and ***L*** show the maximum inward current recorded from a $V_h = -90$ mV. Note that for clarity, only alternate traces from ***D*** to ***F*** are displayed in the top panels of ***G*** to ***I***. GCL, Ganglion cell layer. Scale bar: ***C*** (for ***A–C***), 10 μm. Error bars represent ±1 SEM.

~300 μm on a vibratome (Leica Microsystems). Slice recordings were performed in light-adapted retina. Retinal regions superior or inferior to the optic nerve were typically used.

Slices were transferred to the recording chamber, stabilized with a slice anchor, and continuously perfused with bicarbonate-buffered Ames medium equilibrated with 95% O_2/5% CO_2, pH 7.4, at 31–33°C. Patch-clamp electrodes (9–12 MΩ) were wrapped with Parafilm to reduce pipette capacitance. Electrodes were filled with an intracellular solution comprising the following (in mM): 130 K-methylsulfonate, 8 KCl, 2 Mg_2-ATP, 1 Na-GTP, 1 EGTA, 10 $Na_{0.5}$-HEPES, and ~0.1 Alexa Fluor 488 hydrazide adjusted to pH 7.35 with KOH (osmolarity, 290 mOsm). The liquid junction potential correction for this solution was −10 mV. Tetrodotoxin (TTX, 0.5 μM; Ascent Scientific) and mibefradil (5 μM, Tocris Bioscience) were added to the bath solution.

Currents were filtered at a −3 dB cutoff frequency of 2 kHz by the four-pole Bessel filter of the HEKA EPC-10 patch amplifier, and digitized at 10 kHz. Series resistance (average, 18 ± 9 MΩ; $n = 100$) was compensated on-line to a mean (±SD) level of 58 ± 16%. In all figures, the voltage-activated component of the membrane current was calculated by subtracting appropriately scaled linear current components. The linear current was estimated at the holding potential (V_h) by averaging currents during 16 or 32 ± 5 mV voltage pulses. In the case of the diffuse bipolar cells, the presence of a hyperpolarization-activated cation current (I_h) resulted in a slow outward current relaxation during the +5 mV leak pulse. In these cases, the linear component of the

steady-state current was estimated at the start of the voltage pulse, before the onset of the I_h.

Action potential thresholds were estimated from spikes generated at the onset of depolarizing current pulses of amplitude between 10 and 200 pA in DB3a and DB4 cells. The voltage thresholds were estimated by fitting a line to the upswing region of the depolarization rate (dV/dt) versus V phase plot, and noting where the fitted line intercepted the voltage axis. Spikes were defined as having a peak dV/dt of >10 V/s. The average peak dV/dt of spikes in DB4 and DB3a cells was monotonically distributed with means (±SD) of 32 ± 11 and 16 ± 4 V/s, respectively.

Voltage-gated current analysis. To obtain empirical estimates of the activation range and voltage dependence of voltage-gated currents, leak-subtracted current–voltage (I–V) relations were fit using a Boltzmann equation, assuming ohmic conductance, as follows:

$$I_m = G_{max}(V_m - E_{ion})/(1 + e^{((V_{0.5} - V_m)/z)}),$$

where G_{max} is the maximum conductance, E_{ion} is the reversal potential, $V_{0.5}$ is the half-activation potential, and z is the voltage sensitivity. When fitting the Boltzmann function to the current–voltage relations, a value for the ionic reversal potential was required. For the current measured at the start of depolarizing voltage pulses that were dominated by sodium or calcium channel activation, E_{ion} was allowed to vary during fitting.

Recovery from inactivation of the T-type Ca_V currents was measured at −90 mV. Currents were inactivated by a 500 ms step to −40 mV, followed by a return to −90 mV for a variable time. The T-type current was estimated as the transient component of the current recorded at a −40 mV test potential. The recovery time constant was estimated by fitting an exponential function to the relative amplitude of the T-type current, plotted as a function of the recovery time.

Resting membrane potentials of DB4 cells were measured under current-clamp by setting the current command to 0 A. All analysis was performed with custom routines in Igor Pro (Wavemetrics).

Ganglion cell recordings. Recordings of light-evoked ganglion cell currents were made from intact pieces of nasal retina (eccentricity, ~4–9 mm) with pigment epithelium and choroid attached. Retinae were continuously perfused (~5 ml/min) with bicarbonate-buffered Ames medium equilibrated with 95% O_2/5% CO_2, pH 7.4, at 35°C. The retina was adapted to a background intensity of $\sim 1.5 \times 10^5$ photons/μm^2 ($\lambda = 540$ nm) for at least 30 min before recording. Midget and parasol ganglion cells were initially identified from extracellular spike recordings before whole-cell patch recordings. For whole-cell recordings, the intracellular solution contained the following (in mM): 128 Cs-methylsulfonate, 6 CsCl, 2 Mg-ATP, 1 Na-GTP, 1 EGTA, 10 Na-HEPES, 2.5 Na_2-phosphocreatine, and 3 QX-314, adjusted to pH 7.3 with CsOH and. In some cases, Alexa Fluor 594 hydrazide (0.4 mM) was added to allow morphological inspection. The liquid junction potential correction for this solution was −16 mV. The mean (±SD) dendritic field diameter estimated from fluorescently labeled ON parasol ganglion cells was 210 ± 41 μm ($n = 6$), consistent with previous measurements at comparable eccentricity (Watanabe and Rodieck, 1989; Crook et al., 2008). Cells were stimulated with a 50% positive or negative contrast spot of 250 μm in diameter, which was centered on the receptive field. Contrast was defined as follows: contrast = $(L_{max} - L_{min})/L_{background}$ (where L_{max} is maximum luminance, L_{min} is minimum luminance, and $L_{background}$ is background luminance). The excitatory and inhibitory synaptic conductances elicited by light stimulation were estimated as described previously (Venkataramani and Taylor, 2010; Buldyrev et al., 2012). I–V relations of the net light-evoked currents were measured at 10 ms intervals, and the synaptic conductances were estimated from least-squares fits to these I–V relations at each time point. The synaptic conductances were estimated as the sum of a linear inhibitory conductance (G_{inh}), with a reversal potential at the chloride equilibrium potential (−70 mV) and a linear excitatory conductance (G_{exc}), with a reversal potential at 0 mV. For OFF parasol cells, the I–V relations tended to be nonlinear and bent toward the voltage axis at negative potentials. The nonlinearity could be accommodated with the addition of a third conductance component that had the characteristic voltage dependence of NMDA receptor currents. However, a linear model, as for the ON parasol cells, could also describe the I–V relations adequately. Since the measured effect of TTX on the derived excitatory and inhibitory conductances was essentially the same for the nonlinear and linear fits, we have presented the simpler linear fit results in Figure 11.

Computer models. A stack of confocal images of a DB4 cell were digitized using Neuromantic (http://www.reading.ac.uk/neuromantic/) and were converted to a form suitable for incorporation in the NeuronC simulation package (Smith, 1992). Models were run as described previously (Schachter et al., 2010). The modeling focused on reproducing the voltage-clamp data shown in Figure 1. For the bipolar cells, the specific membrane capacitance was set to 1 $\mu F/cm^2$, and the specific membrane resistivity was set to 30 $k\Omega/cm^2$ to reproduce the average input resistance of DB4 cells. This value is very similar to direct measurements from mouse rod bipolar cells (Oltedal et al., 2009). The default value for the axoplasmic resistivity was 100 Ω/cm. The model was initially calibrated by adding delayed rectifier potassium channels throughout the cell to reproduce the average outward potassium currents observed. $Na_V1.1$ sodium channels, modeled using a published discrete-state Markov scheme (Clancy and Kass, 2004), were added to the AIS region to reproduce the amplitude of the action currents observed. The model worked well for values of axonal resistivity (R_i) similar to those that have been measured directly from retinal bipolar cells (Oltedal et al., 2009).

In the absence of channels in the soma and proximal dendrites, the amplitude of the action currents remained constant with increasing depolarizing steps, before declining as the driving force on the Na_v current decreased. In real cells, the maximum inward current first increased and then decreased as a function of the step potential. In effect, the unclamped action currents appeared to be superimposed on well clamped Na_v currents. The addition of a low level of Ca_v channels to well clamped regions, close to the recording electrode (soma, dendrites, and proximal axon) was essential to reproduce this behavior. The density of channels required, ~10–20 pS/μm^2, was somewhat lower than estimates for somatic membranes in other central neurons (Kole and Stuart, 2012).

Statistical Analysis. Paired two-tailed t tests were used for comparisons of ganglion cell conductances. An α level of 0.05 was used.

Results

Bipolar cells of the magnocellular pathway exhibit Na_v and T-type Ca_v currents

Our first objective was to look for evidence for selective expression of Na_V and T-type Ca_V channels in bipolar cells that make input to the ON and OFF type parasol ganglion cells (magnocellular pathway). To address this aim, we recorded voltage-gated currents from bipolar cells in macaque retinal slices by applying a series of depolarizing voltage steps from a V_h of −70 or −90 mV. The bipolar cells were filled with fluorescent dye so that they could be anatomically classified, according to the scheme of Boycott and Wässle (1991), at the conclusion of the recordings.

We first examined currents in DB3 cells, which provide the major input to the OFF-type parasol ganglion cell (Jacoby et al., 2000; Calkins and Sterling, 2007). We found that morphologically identified DB3 cells comprised two functionally distinct subtypes, which we designate herein as DB3a and DB3b. Both DB3a and DB3b cells had bulbous axon terminal boutons that stratified at ~28–32% (stratum 2) depth of the IPL (Fig. 1*A*,*B*. A 0% depth exists at the border of the INL and the IPL, and a 100% depth is the border of the IPL and the ganglion cell layer.

We identified three major functional differences between DB3a and DB3b cells. First, during depolarizing steps from −70 mV, DB3a cells exhibited a prominent transient inward current at the beginning of depolarizing steps positive to −60 mV, with a maximum amplitude of −415 ± 50 pA near −20 mV ($n = 20$; Fig. 1*D*,*G*,*J*). This current was mediated by Na_V channels, since it was completely blocked by bath application of TTX (0.5 μM, $n = 4$; Fig. 1*G*,*J*). In contrast, the DB3b cells showed much smaller,

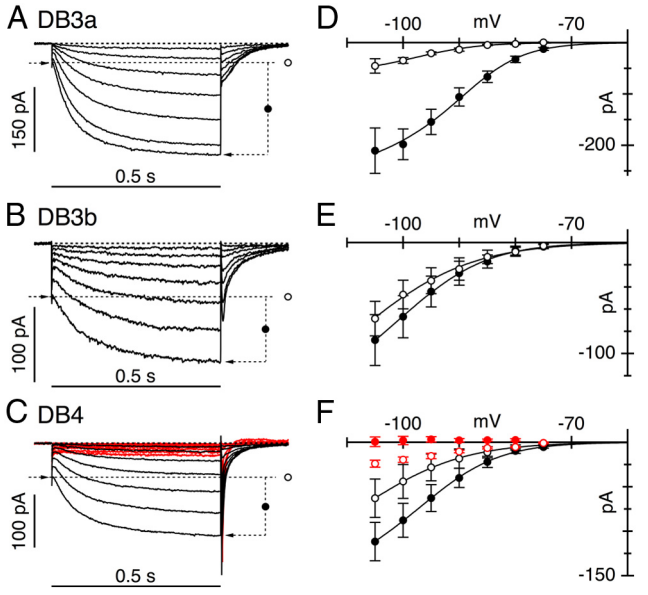

Figure 2. Bipolar cells of the magnocellular pathway display rapidly activating I_hs. ***A–C***, $V_h = -70$ mV. Average leak-subtracted currents activated by 500 ms hyperpolarizing voltage steps from −75 to −105 mV in 5 mV increments in DB3a (***A***), DB3b (***B***), and DB4 (***C***) cells. The red traces in ***C*** are recorded in the presence of CsCl. ***D–F***, Current–voltage relations showing the peak instantaneous currents (open symbols) and time-dependent (I_h) currents (closed circles) for DB3a ($n = 13$), DB3b ($n = 12$), and DB4 ($n = 21$) cells. Red symbols in ***F*** show currents in the presence of CsCl ($n = 5$). Error bars represent ±1 SEM.

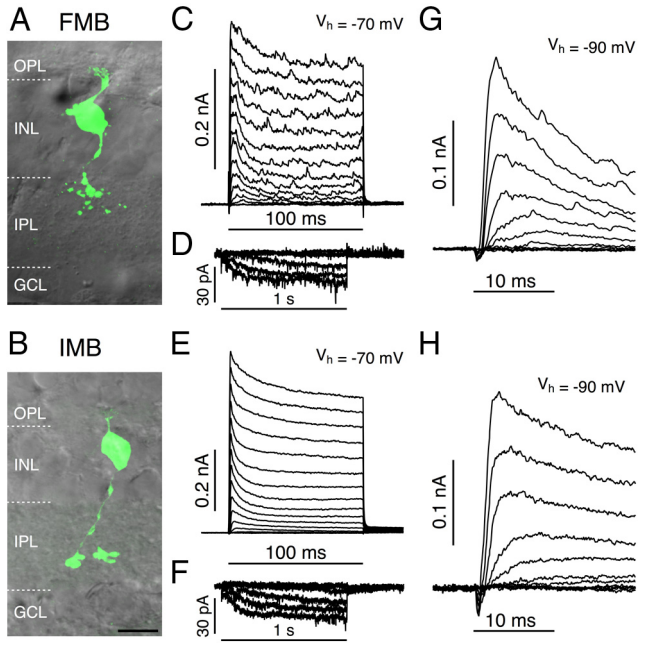

Figure 3. Midget bipolar cells lack prominent Na_V, T-type Ca_V, or I_hs. ***A***, ***B***, Confocal projections showing examples of recorded FMB (***A***) and IMB (***B***) cells overlayed on a transmitted light image of the same field. Retinal layers are indicated to the left of the panels. ***C***, $V_h = -70$ mV. Voltage-activated currents recorded during 100 ms depolarizing voltage steps from −65 to +10 mV in 10 mV increments. Traces are averages from 19 FMB cells. ***D***, $V_h = -70$ mV. Average leak-subtracted currents activated by 500 ms hyperpolarizing voltage steps from −75 to −100 mV in 5 mV increments. Traces are averages of six FMB cells. ***E***, Voltage-activated currents recorded during voltage steps as in ***C***. Traces are averages from 42 IMB cells. ***F***, $V_h = -70$ mV. Voltage-activated currents recorded during voltage steps as in ***D***. Traces are averages of six IMB cells. ***G***, ***H***, $V_h = -90$ mV. Voltage-activated currents at the onset of voltage steps between −80 and −30 mV in 10 mV increments in FMB (***G***) and IMB (***H***) cells. Traces are averages of $n = 3$ for each cell type. Note that little transient inward current is activated in midget bipolar cells, suggesting a lack or low density of Na_V or T-type Ca_V currents. Scale bar: ***B*** (for ***A*** and ***B***), 10 μm.

more sustained inward currents during identical depolarizing steps (peak amplitude, −73 ± 11 pA near −20 mV; $n = 13$; Fig. 1*E*,*H*,*K*). The second functional difference was revealed during depolarizing steps from the more negative holding potential of −90 mV. The peak inward current became larger in DB3a cells (1.6 ± 0.16 nA; $n = 10$; Fig. 1*G*) but was completely blocked by TTX, indicating that the larger amplitude was due to removal of the inactivation of Na_V channels. DB3b cells also produced a larger peak inward current when depolarized from −90 mV (−410 ± 40 pA; $n = 10$; Fig. 1*H*,*K*); however, the currents had a lower threshold and were slower to activate and inactivate compared with DB3a cells (Fig. 1*H*). The activation range and kinetics of this current appeared consistent with T-type Ca_V3 channels. In an effort to identify the Ca_V3 subunit involved, we measured the rate of recovery from inactivation (see Materials and Methods), which is considerably faster for $Ca_V3.1$ ($\tau \sim 117$ ms) than for $Ca_V3.2$ ($\tau \sim 395$ ms) and $Ca_V3.3$ ($\tau \sim 352$ ms) channels (Perez-Reyes, 2003). Recovery time constants were 91 and 113 ms in two cells, consistent with the presence of $Ca_V3.1$ channels. This identification is corroborated by the immunohistochemical data shown below (see Fig. 7). The third functional difference was the magnitude of the sustained outward currents that activated positive to approximately −40 mV in DB3 cells (Fig. 1*D*,*E*). These currents, presumably representing the ubiquitous outward rectifier potassium current, were almost fourfold larger in DB3a than DB3b cells. Overall, these results identify two functionally distinct DB3 cells that likely make input to OFF parasol ganglion cells, DB3a cells that display large Na_V currents, and DB3b cells, which show large T-type Ca_V currents.

If the presence of regenerative T-type Ca_V and Na_V currents is important for tuning inputs to parasol ganglion cells, then one would expect that similar currents should be observed in the bipolar cells presynaptic to the ON-type parasol ganglion cells. Thus, we analyzed currents from DB4 cells (Fig. 1*C*), which, based on their stratification at 50–58% (stratum 3) of the IPL, are thought to provide input to ON parasol ganglion cells (Boycott and Wässle, 1991; see also Figs. 11, 12). The DB4 cells shared properties with both the DB3a and DB3b cells. Similar to the DB3a cells, depolarization of DB4 cells from −70 mV elicited large transient inward currents (peak amplitude, −225 ± 21 pA near −20 mV; $n = 34$ cells; Fig. 1*F*,*I*) that were suppressed by bath application of 0.5 μM TTX (residual amplitude, −9 ± 3 pA; $n = 8$ cells; Fig. 1*I*,*L*). Similar to the DB3b cells, depolarization of DB4 cells from −90 mV enhanced the maximum inward current (−874 ± 108 pA, $n = 8$), which became slower to activate and inactivate. The enhanced inward current was due in part to recruitment of T-type Ca_V channels, since it was only partially blocked by TTX (to −271 ± 39 pA; $n = 5$; Fig. 1*I*,*L*) and was sensitive to mibefradil, a T-type Ca_V channel blocker (5 μM, $n = 3$; Fig. 1*I*). The combined application of mibefradil and TTX completely blocked all transient inward currents activated from −90 mV (Fig. 1*I*,*L*; $n = 2$). Like the DB3b cells, the recovery from inactivation for the T-type currents, measured in the presence of TTX, was also relatively rapid (mean ± SEM, 52 ± 8 ms; $n = 4$), consistent with the presence of $Ca_V3.1$ channels (Perez-Reyes, 2003).

Since bipolar cells are relatively small neurons, we expected to be able to adequately voltage-clamp the Na_V and Ca_V currents. Thus, we were surprised to observe "action currents" in DB3a and DB4 cells occurring with variable delay after the onset of

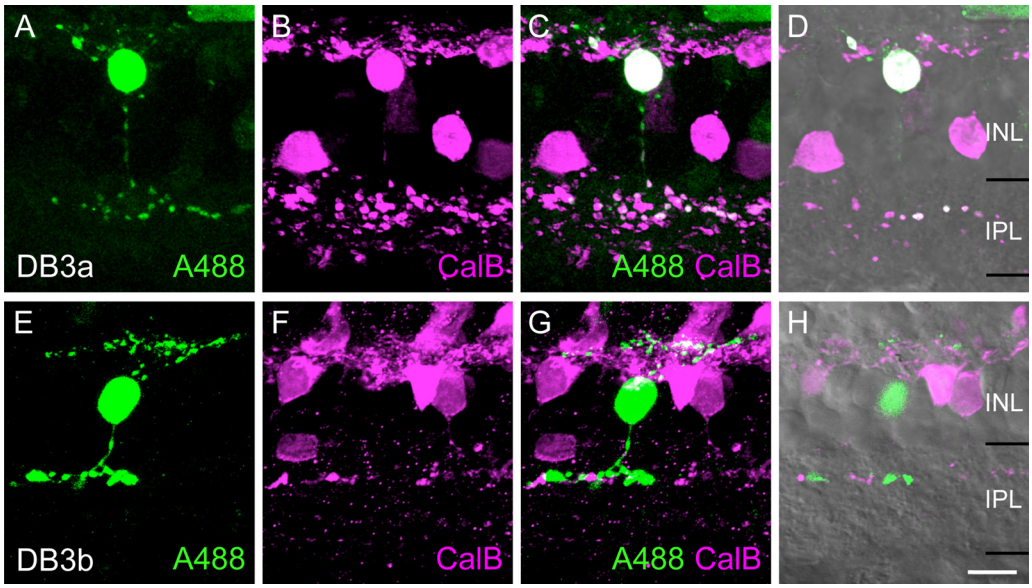

Figure 4. DB3a and DB3b cells can be distinguished using immunohistochemical markers. ***A–C***, Confocal projection of a physiologically identified DB3a cell filled with Alexa Fluor 488 (A488, ***A***) and subsequently labeled for calbindin (CalB, ***B***). The merged image in ***C*** shows that DB3a cells are CalB immunoreactive. ***D***, Single confocal plane focused on axon terminals overlayed on transmitted light image to show axon terminal stratification. ***E–H***, Confocal projection of a physiologically identified DB3b cell filled with Alexa Fluor 488. The DB3b cell lacks CalB immunoreactivity (***F***; merged in ***G***). DB3b axon terminals stratify at a comparable depth to DB3a (***H***). Scale bar, 10 μm.

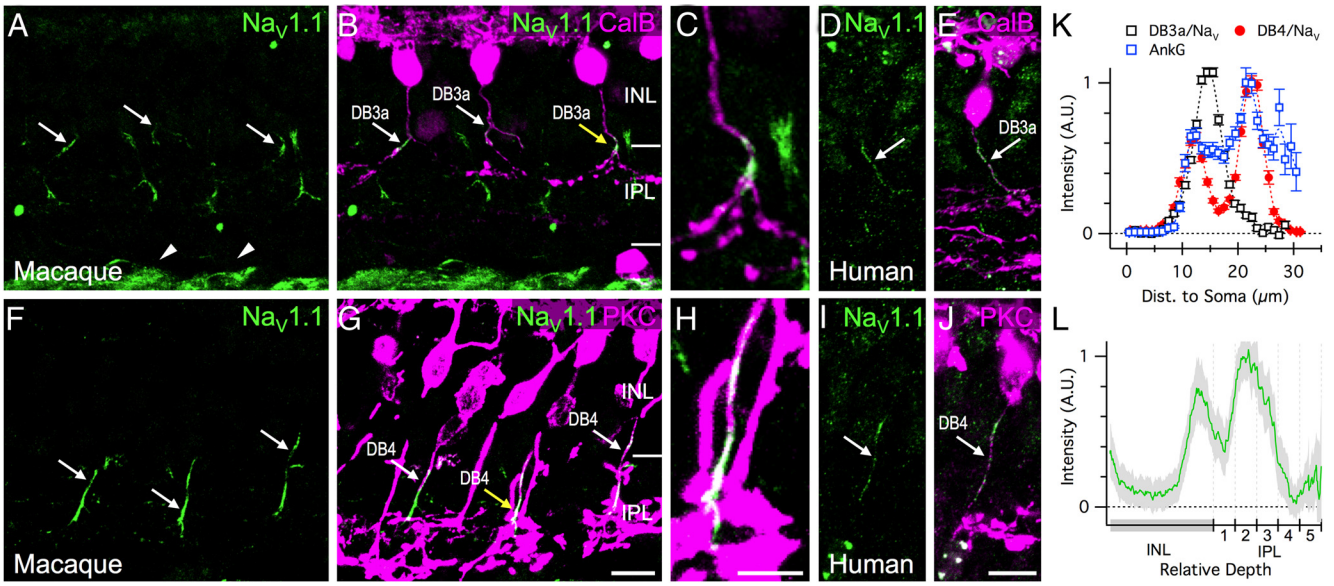

Figure 5. $Na_V1.1$ clusters in the distal axon of magnocellular pathway bipolar cells. ***A–E***, Confocal micrographs showing $Na_V1.1$ concentrated in the distal axon near the axonal branch-point of CalB-positive DB3a cells of the macaque (arrows, ***A***, ***B***) and human (arrows, ***D***, ***E***) retinae. Note that ganglion cell axons are also labeled for $Na_V1.1$ (***A***, arrowheads). The DB3a axon indicated by the yellow arrow in ***B*** is shown enlarged in ***C***. ***F–J***, $Na_V1.1$ concentrated in the distal axon and in the axonal branch point of PKCα (PKC)-positive DB4 cells of the macaque (arrows, ***F***, ***G***) and human (arrows, ***I***, ***J***) retinae. The axon indicated by the yellow arrow in ***G*** is shown enlarged in ***H***. ***K***, Graph showing relative fluorescence intensity (arbitrary units) of $Na_V1.1$ in DB3a and DB4 axons, and AnkG in DB4 axons, relative to the position of the soma. Note the bimodal distribution of $Na_V1.1$ in DB4 cells. Error bars represent ± 1 SEM. ***L***, Average relative $Na_V1.1$ intensity measured as a function of retinal depth. Gray shading shows 95% CI ($n = 3$ retinae). Retinal depth is shown beneath the graph, and numbers denote strata 1–5 of the IPL. Note the reduction in $Na_V1.1$ staining in the S1 region of IPL. Scale bars: ***G*** (for ***A***, ***B***, ***F***, ***G***), 10 μm; ***H*** (for ***C***, ***H***), 5 μm; ***J*** (for ***D***, ***E***, ***I***, ***J***), 10 μm.

depolarizing voltage steps near the threshold for channel activation. Such events are most likely a result of inadequate voltage control due to activity of Na_V channels at a distance from the recording electrode. Nonetheless, an empirical estimate of the activation range of the Na_V channels in DB3a and DB4 cells was obtained by fitting the average peak currents from a large sample of cells (20 DB3a cells and 34 DB4 cells) with a Boltzmann function (Fig. 1*J*,*L*, continuous lines; see Eq. 1 in Materials and Methods). The fitted lines indicate that the activation range was very similar in the two cell types (DB3a: $V_{0.5} = -39$ mV, $z = 5.0$ mV, Fig. 1*J*; DB4: $V_{0.5} = -39$ mV, $z = 4.6$ mV, Fig. 1*L*). In contrast to the Na_V currents, the T-type Ca_V currents in DB3b and DB4 cells appeared to be well voltage-clamped, as expected for channels located close to the recording electrode. The Boltzmann fits to the T-type currents showed similar activation parameters between DB3b and DB4 cells (DB3b: $V_{0.5} = -58$ mV, $z = 4.2$ mV, Fig. 1*K*; DB4: $V_{0.5} = -54$ mV, $z = 5.5$ mV; Fig. 1*L*). The differential localization of the Na_V and Ca_V channels expressed in DB3a/b

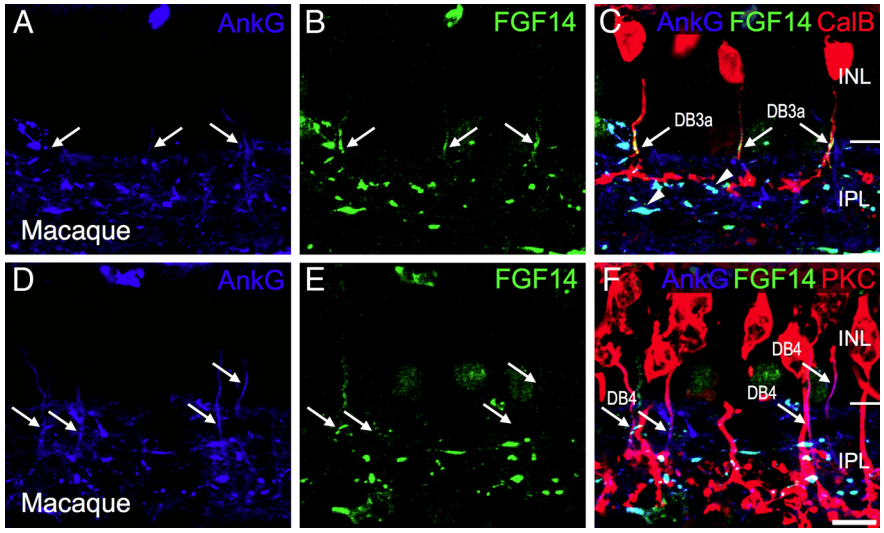

Figure 6. Bipolar cells of the magnocellular pathway possess an axon initial segment-like region. Confocal images of macaque retina labeled for axon initial segment proteins. ***A–C***, Triple label for AnkG (blue), FGF-14 (green), and the DB3a-marker CalB (red). Merged image is shown in ***C***. Arrows indicate regions on DB3a axons where FGF-14 staining is most concentrated. Note that very weak AnkG staining was also present in the DB3a axons. ***D–F***, Triple label for AnkG (blue), FGF-14 (green), and PKCα (red). Strong AnkG staining was evident in DB4 axons, but FGF-14 immunoreactivity was undetectable (arrows). Note that FGF-14 and AnkG were present in other short profiles in the IPL that likely represent amacrine cell AISs (arrowheads in C). Scale bar: ***F*** (for all panels), 10 μm.

and DB4 cells is further corroborated by the immunohistochemical data provided below.

We also analyzed each of the other diffuse bipolar cell types described by Boycott and Wässle (1991): DB1 ($n = 9$), DB2 ($n = 16$), DB5 ($n = 24$), and DB6 ($n = 7$). None of these exhibited large Na_V currents from a holding potential of −70 mV, but DB2 and DB5 cells showed evidence of T-type currents (data not shown). In addition, we encountered two putative "giant bipolar cells," which stratify at the same depth as DB4 (Joo et al., 2011). These cells displayed Na_V currents similar to DB4 cells, but lacked T-type currents from a holding potential of −90 mV (data not shown). Overall, these results demonstrate that high densities of Na_V channels are a distinguishing feature of diffuse bipolar cells that make input to the magnocellular pathway.

Bipolar cells of the magnocellular pathway exhibit large I_hs

I_hs have been associated with more transient responses in photoreceptors (Barrow and Wu, 2009) and with the temporal tuning of spiking behavior in other neurons (Hutcheon et al., 1996; Hutcheon and Yarom, 2000). Therefore, we were interested to determine whether I_hs might be coexpressed in cells that display Na_V currents within transient signaling pathways. We tested for the presence of I_hs by applying hyperpolarizing voltage steps from a holding potential of −70 mV. Two nonlinear current components were identified, as follows: an instantaneous component, likely reflecting current through inwardly rectifying K^+ channels; and a time-dependent component, indicative of the activation of I_h channels. The instantaneous component was evaluated as the current amplitude 4 ms after the onset of the voltage step, and the I_h component was evaluated as the increase in the inward current during the voltage step (Fig. 2*A–C*). At −105 mV, the average I_h component was well described by the sum of two exponentials, with activation time constants in the DB3a, DB3b, and DB4 cells ($\tau_{fast} = 42$, 58, and 57 ms; $\tau_{slow} = 158$, 357, and 332 ms, respectively) that were comparable to those reported previously for HCN1 channels (Müller et al., 2003). The activation parameters, obtained from fitting the Boltzmann function to the maximum inward I_hs, were similar in the three cell types (Fig. 2*D–F*; DB3a, DB3b, DB4 cells, respectively: $V_{0.5} = -78$, −90, −84 mV; $z = 6.3$, 6.5, 7.0 mV). The I_hs could be completely blocked by 4 mM extracellular CsCl (Fig. 2*C*,*F*; $n = 5$). Of the diffuse bipolar cells, only DB3a, DB3b, and DB4 cells displayed rapidly activating I_hs, suggesting a selective role for these channels in transient signaling pathways.

Bipolar cells of the parvocellular pathway lack Na_v, T-type Ca_v, and I_hs

If the presence of Na_V, T-type Ca_V, and I_hs is important for signaling within transient visual pathways, then one would expect a lack of such currents in the FMB (Fig. 3*A*) and IMB (Fig. 3*B*) cells, which provide input to the OFF and ON parvocellular (midget) ganglion cells respectively (Polyak, 1941; Kolb and Dekorver, 1991; Calkins et al., 1994). Consistent with this prediction, depolarizing voltage steps did not elicit significant inward currents in FMB or IMB cells, from a holding potential of either −70 mV (Fig. 3*C*,*E*) or −90 mV (Fig. 3*G*,*H*). Depolarizing pulses activated large outward potassium currents; however, unlike diffuse cells (Fig. 1*D–F*), the potassium currents in FMB and IMB cells showed partial inactivation during the voltage steps (Fig. 3*C*, $n = 19$ FMB cells; Fig. 3*E*, $n = 42$ IMB cells). A notable difference between the outward currents in FMB and IMB cells was the presence of more current variance in the FMB cells (Fig. 3*C*,*E*, compare traces), which was due to the presence of spontaneous glycinergic IPSCs in FMB cells that were sensitive to strychnine (data not shown). Hyperpolarizing pulses in FMB and IMB cells failed to elicit large I_hs; peak inward currents were less than ~25 pA at −105 mV (Fig. 3*D*,*F*). Moreover, unlike DB3a/b or DB4 cells, there was little inward rectification of the instantaneous current at the onset of a voltage step. Notably, the smaller midget bipolar cells had resting input resistances (Rinput) twofold to threefold higher than the corresponding diffuse bipolar cells of the magnocellular pathway (FMB cells: $R_{in} = 1.42 \pm 0.17$ GΩ, $n = 19$; DB3a cells: $R_i = 0.415 \pm 0.05$ GΩ, $n = 12$; IMB cells: $R_i = 1.00 \pm 0.07$ GΩ, $n = 41$; DB4 cells: $R_i = 557 \pm 70$ MΩ, $n = 34$). Overall, we conclude that Na_V, T-type Ca_V, and HCN channels are weakly expressed or absent from midget bipolar cells and are therefore unlikely to contribute substantially to the intrinsic membrane properties of these cells.

DB3a and DB3b cells can be distinguished using immunohistochemical markers

Previous studies have demonstrated that a DB3-like cell expresses the calcium-binding protein CalB and provides synaptic input to OFF parasol ganglion cells (Jacoby and Marshak, 2000). To determine whether this cell type corresponded to DB3a or DB3b cells, we performed immunohistochemistry on retinal slices after filling cells with fluorescent dye during single-cell recordings (Fig. 4). We found that the cells we have denoted DB3a correspond to the CalB-positive DB3 cells, which have been anatomically characterized in previous studies (Grünert et al., 1994; Jacoby et al., 2000). By contrast, DB3b cells lacked CalB immu-

noreactivity, and thus likely represent the CalB-negative, CaBP5-positive, DB3-like cells that have been identified in human and macaque retinae (Haverkamp et al., 2003). We used these markers to determine the localization of voltage-gated channel subunits in DB3a and DB3b cells, as detailed below.

$Na_V1.1$ is clustered at an AIS-like region of DB3a and DB4 cells

We used immunohistochemistry to determine the subunit composition and subcellular location of the Na_V channels in DB3a and DB4 cells. Since we observed unclamped action currents during our voltage-clamp experiments, we expected to localize channels at sites remote from the somatic compartment. Immunostaining for the Na_V channel α subunit, $Na_V1.1$, revealed labeling in radially aligned processes in the inner nuclear layer and inner plexiform layer (Fig. 5*A*,*F*). Double-labeling experiments with immunohistochemical markers for DB3a and DB4 cells (see Fig. 13 and Materials and Methods) revealed that $Na_V1.1$ was localized in the axons of both DB3a cells (Fig. 5*B*,*C*) and DB4 cells (Fig. 5*G*,*H*), with highest immunoreactivity in the distal axon and the axonal branch points. $Na_V1.1$ was not detected in the axon terminal boutons. All of the $Na_V1.1$-labeled processes in the INL/IPL colocalized with DB3a or DB4 cells, corroborating the physiological results showing large Na_V currents exclusively in these bipolar cell types. In addition, $Na_V1.1$ was present in ganglion cell axons (Fig. 5*A*,*B*), as has been shown previously in the rat retina (Van Wart et al., 2005). We also examined whether Na_V channel staining was conserved in homologous bipolar cells of the human retina. Indeed, as in the macaque retina, we found $Na_V1.1$ concentrated in the axons of both DB3a (Fig. 5*D*,*E*) and DB4 (Fig. 5*I*,*J*) cells.

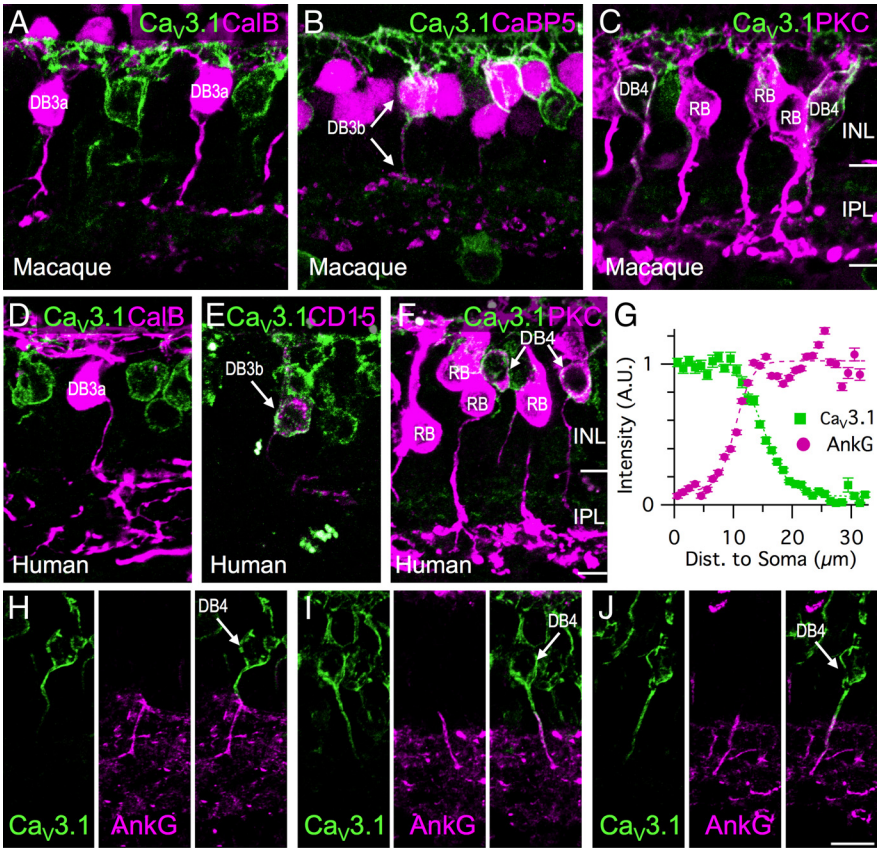

Figure 7. $Ca_V3.1$ is concentrated in the somatodendritic compartment and proximal axon of magnocellular pathway bipolar cells. ***A***, Absence of $Ca_V3.1$ immunoreactivity in CalB-positive DB3a cells. ***B***, $Ca_V3.1$ immunostaining in the somatodendritic compartment and proximal axon of CaBP5-positive DB3b cells (soma and axon terminals indicated by top and bottom arrow, respectively). ***C***, $Ca_V3.1$ immunostaining in the somatodendritic compartment and proximal axon of PKCα-positive DB4 cells (white regions). Note that PKCα-positive rod bipolar cells (RB) lack $Ca_V3.1$. ***D–F***, $Ca_V3.1$ is present in CD15-positive DB3b cells (***E***) and PKCα-positive DB4 cells (***F***) of the human retina but is absent from CalB-positive DB3a cells (***D***). ***G***, Average fluorescence profiles for $Ca_V3.1$ and AnkG in 23 DB4 cells from three macaque retinae. Profiles were aligned to the start of the AnkG staining. Note the decline in $Ca_V3.1$ immunoreactivity as AnkG immunoreactivity increases. ***H–J***, Examples of macaque DB4 cells labeled for $Ca_V3.1$ (left panels) and AnkG (middle panels). Right panels, Merged images illustrate the transition between $Ca_V3.1$ and AnkG immunoreactivity down the axon. Note that these cells were confirmed to be DB4 cells by triple labeling for PKCα, but for simplicity, the PKCα channel is not shown. Scale bar: ***J*** (for all panels), 10 μm.

Our results differed from previous studies in rodent retinae, which found $Na_V1.1$ in AIS-like segments of AII amacrine cells, but not in bipolar cells (Van Wart et al., 2005; Wu et al., 2011). In light of this apparent discrepancy, we repeated $Na_V1.1$ staining in rat and mouse retinae under identical experimental conditions to those that we used for the primate, and found that $Na_V1.1$ localization was consistent with earlier reports (i.e., $Na_V1.1$ was in amacrine cell AISs but not in bipolar cell axons; data not shown). Thus, the expression of a high density of $Na_V1.1$ in bipolar cell axons appears to be a specialization of primate retinae. We also immunostained for $Na_V1.2$ or $Na_V1.6$, two other Na_V subunits that are commonly found in central neurons, but neither subunit was detected in primate or rodent bipolar cells (data not shown).

The precise subcellular localization of Na_V channels is critical for determining neuronal excitability (Kole and Stuart, 2012), and thus we quantified the position of the axonal $Na_V1.1$ channels relative to the DB3a and DB4 cell somata (see Materials and Methods). The average $Na_V1.1$ intensity in DB3a cells was characterized by a peak located ~14 μm from the soma, with a width at half-height of ~7 μm ($n = 31$; Fig. 5*K*). In DB4 cells, the average $Na_V1.1$ profile was bimodal ($n = 20$; Fig. 5*K*), with two segments also evident in individual DB4 axons (Fig. 5*F*). These peaks were positioned at ~12 and ~23 μm from the soma, and each segment was ~6–7 μm wide. The gap in the DB4 staining appeared to coincide spatially with the S1 region of the IPL. Indeed, when we quantified $Na_V1.1$ intensity as a function of retinal depth (Fig. 5*L*), we found that the outer peak, which comprised staining from both DB3a and DB4 cells, was located in the inner aspect of the INL, while the second peak comprising staining from the inner segment of DB4 cells was located at an ~40% depth of the IPL, corresponding to S2. The S1 region showed a marked reduction of $Na_V1.1$ immunoreactivity, suggesting that $Na_V1.1$ expression might be regulated by extrinsic factors.

The concentration of $Na_V1.1$ channels in a defined region of the axon was reminiscent of the Na_V clustering seen in the AIS of spiking central neurons. Therefore, we tested for the presence of two AIS-associated proteins: AnkG, a scaffolding protein that clusters Na_V channels (Kordeli et al., 1995; Zhou et al., 1998); and FGF-14, a modulator of Na_V channel function (Lou et al., 2005). AnkG was detected in the axons of both DB3a (Fig. 6*A*,*C*) and DB4 cells (Fig. 6*D*,*F*), but expression levels were higher in DB4

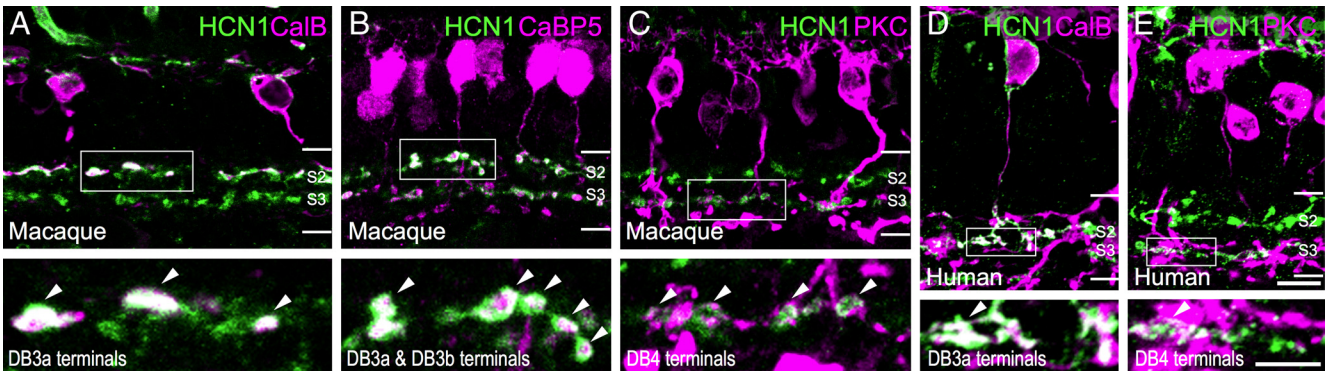

Figure 8. HCN1 is concentrated in the axon terminal boutons of magnocellular pathway bipolar cells. ***A–E***, Confocal images showing HCN1 (green) immunoreactivity in the macaque (***A–C***) and human retina (***D***, ***E***). Rectangular regions of interest are shown at higher magnification in the bottom. HCN1 immunoreactivity was concentrated in two prominent bands located in S2 and S3 of the IPL. ***A***, The HCN1 staining in S2 is localized to the axon terminal boutons of CalB-positive DB3a cells (arrowheads). Note that some axon terminals in S2 are not CalB-positive. These terminals belong to DB3b cells. ***B***, All HCN1 staining in S2 colocalizes with CaBP5, indicating expression by both DB3a and DB3b cells (arrowheads). ***C***, The HCN1 staining in S3 is localized to the axon terminal boutons of PKCα-positive DB4 cells (arrowheads). ***D***, ***E***, HCN1 is present in axon terminal boutons of CalB-positive DB3a cells (***D***) and PKCα-positive DB4 cells (***E***) in the human retina (arrowheads). Scale bars: ***E*** top (for top panels), 10 μm; ***E*** lower (for lower panels), 5 μm.

cells. In contrast, FGF-14 was strongly expressed in DB3a cells (Fig. 6*B*,*C*) but was absent from DB4 cells (Fig. 6*E*,*F*). AnkG and $Na_V1.1$ fluorescence intensity profiles aligned precisely on the DB4 cells; however, AnkG was more uniformly distributed along the axon (Fig. 5*K*). In contrast to $Na_V1.1$, AnkG and FGF-14 were not found exclusively in bipolar cell axons, but were also observed in other short processes that likely include amacrine cell AISs (Wu et al., 2011). Overall, these results demonstrate that primate DB3a and DB4 cells express $Na_V1.1$ channels in an AIS-like compartment, but that the molecular composition of the AIS differs between these two cell types.

$Ca_V3.1$ channels are expressed in the somatodendritic compartment and proximal axon of magnocellular pathway bipolar cells

The localization of the T-type Ca_V currents observed in DB4 and DB3b cells (Fig. 1) could influence the functional role of these channels. For example, somatodendritic T-type channels could contribute to integration and boosting of synaptic inputs (Perez-Reyes, 2003), whereas channels localized to the axon terminals might contribute to transmitter release, as has been shown previously in some rat bipolar cells (Pan et al., 2001). Thus, we sought to establish the subunit identity and cellular localization of the T-type channels. We found prominent immunoreactivity for the T-type Ca_v subunit $Ca_V3.1$ in the somatodendritic compartment and proximal axon of a subset of diffuse bipolar cells (Fig. 7), but no immunostaining was evident in the axon terminal boutons. In accordance with our electrophysiological results (Fig. 1), we found that $Ca_V3.1$ (α1G) was present on DB3b cells and DB4 cells (Fig. 7*B*,*C*), but was absent from DB3a cells (Fig. 7*A*). $Ca_V3.1$ immunostaining was absent from FMB and IMB cells (data not shown), consistent with the electrophysiological findings (Fig. 3). We found that the expression pattern of $Ca_V3.1$ was essentially the same in human retina, with expression in DB3b and DB4 cells, but not DB3a cells (Fig. 7*D–F*). We did not detect $Ca_V3.2$ immunoreactivity in primate bipolar cells (data not shown). Together with the electrophysiological results, these findings suggest that somatodendritic $Ca_V3.1$ mediates the T-type currents observed in DB3b and DB4 cells.

We were interested to find that, in addition to the somatodendritic staining, $Ca_V3.1$ was present in the proximal axon of DB3b and DB4 cells. Previous calcium imaging studies indicate that T-type Ca_V channels are present in the AISs of some central neurons, where they influence spike shape and initiation (Bender and Trussell, 2009). T-type channels may also modulate the length and location of the AIS in response to neuronal activity (Grubb and Burrone, 2010). In light of these prior studies, we quantified the localization of $Ca_V3.1$ channels, relative to the AIS, by making profile plots of fluorescence intensity down the length of the DB4 axons (see Materials and Methods). The results revealed an interesting pattern, whereby $Ca_V3.1$ immunoreactivity was maximal in the proximal part of the axon and began to decline at a position corresponding to the start of the AIS (Fig. 7*G*). This relationship is clearly evident in individual DB4 axonal profiles (Fig. 7*H–J*). The results lend support to the idea that Ca_V3 channel activation could be important for determining the localization of the AIS in bipolar cells.

HCN1 channels are concentrated in axon terminal boutons of magnocellular pathway bipolar cells

Next, we looked for evidence of the selective expression of HCN channel subunits in bipolar cells that provide input to the magnocellular pathway. The rapid gating time constants for I_hs suggested the presence of the HCN1 subunit in DB3a/b and DB4 cells. Consistent with these physiological results, immunostaining for HCN1 channels revealed two prominent bands of axon terminal boutons located in S2 and S3 of the IPL (Fig. 8*A–C*). Double labeling with bipolar cell markers showed that some HCN1-positive terminals in S2 belonged to DB3a cells (Fig. 8*A*), while the remainder represent DB3b axon terminals (Fig. 8*B*). The band of HCN1-positive terminals in S3 of the IPL corresponded to axon terminal boutons of DB4 cells (Fig. 8*C*). The soma and dendrites of DB3a cells were also weakly immunoreactive for HCN1 (Fig. 8*A*). The localization of the HCN1 subunit was comparable in homologous bipolar cells of the human retina (Fig. 8*D*,*E*). These results demonstrate that the HCN1 channel subunit is mainly concentrated in axon terminal boutons of bipolar cells that provide input to magnocellular pathways.

DB3a and DB4 cells generate action potentials in response to current injection

The presence of Na_V and T-type Ca_V currents suggests that DB3a and DB4 cells might generate action potentials or nonlinear voltage responses. To test this idea, we recorded bipolar cell voltage responses in current-clamp. From −70 mV, both DB3a and DB4

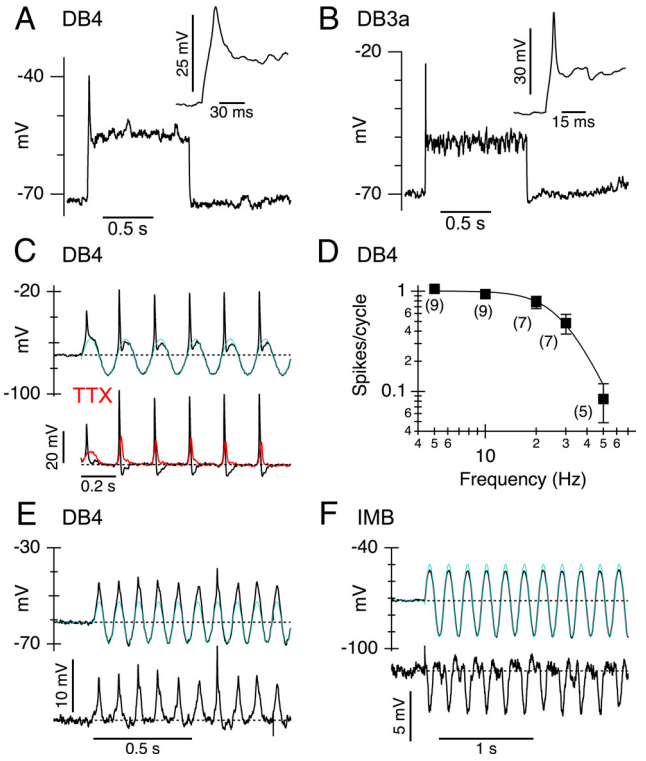

Figure 9. Action potentials can be elicited in DB3a and DB4 cells. ***A***, ***B***, Spikes initiated at the onset of depolarizing current injections in DB4 (***A***, 20 pA) and DB3a (***B***, 50 pA) cells. The inset shows an expanded timescale. ***C***, Voltage generated in DB4 cells by 5 Hz sinusoidal current injections with a peak-to-peak amplitude of 20 pA. Action potentials were elicited during the positive phase of each cycle. The cyan lines show the sine function fit to the negative phase. The sine fits were subtracted to reveal the nonlinear component of the voltage response (***C***, bottom). Spikes of ~40 mV in amplitude in control became smaller and broader in the presence of TTX (***C***, red trace). ***D***, Average number of spikes per stimulus cycle for a range of stimulus frequencies (number of cells averaged). The smooth curve through the points predicted the number of spikes per cycle dropped by half at 28 Hz. ***E***, ***F***, Current-clamp recording from a DB4 cell during a 10 Hz, 20 pA peak-to-peak sine wave current injection. The resting potential (zero current command) was −61 mV. The cyan lines show the sine function fit to the negative phase. The sine fits were subtracted to reveal the nonlinear component of the voltage response during the depolarizing phase (***E***, lower). ***F***, Average voltage response for six IMB cells during 5 Hz current stimulation. The cells were hyperpolarized by current injection to produce an average resting potential of approximately −70 mV. Subtraction of the sine function fit to the negative phase (cyan overlay) revealed slightly sublinear voltage responses during the positive phase (lower trace), presumably due to activation of voltage-gated potassium currents.

cells generated single action potentials at the onset of a depolarizing current step (Fig. 9*A*,*B*). The mean (±SEM) action potential thresholds were −53.0 ± 1.7 mV (DB3a cells, $n = 5$) and −58.1 ± 1.6 mV (DB4 cells, $n = 11$). DB3a and DB4 cells produced only a single spike during depolarizing pulses. We wanted to determine whether they could fire more frequently, as might be required to signal a high-contrast, flickering stimulus. We tested this idea by applying sinusoidal current injection at a range of frequencies relevant to the expected physiological range. DB4 cells generated action potentials during the depolarizing phase of the current injection (Fig. 9*C*). The waveforms of action potentials are illustrated more clearly by subtracting a sine-wave fitted to the linear negative phase of the voltage signal (Fig. 9*C*, bottom). After the first half cycle, action potentials became larger, presumably due to removal of some Na_V channel inactivation during the negative phase of the stimulus. Action potentials were smaller and broader in the presence of TTX (0.5 μM), and the residual nonlinearity was likely driven by the slower kinetics of the T-type Ca_V currents (Fig. 9*C*). At low frequencies, DB4 cells generally entrained perfectly, firing once per stimulus cycle, but the entrainment declined as the stimulus frequency increased (Fig. 9*D*), and dropped to 0.5 spikes/cycle at ~30 Hz. We estimated the precision of spike timing by measuring the SD of the spike times relative to the onset of each stimulus cycle, and obtained values of 2.9 ± 1.0 ms at 5 Hz ($n = 10$) and 1.8 ± 1.1 ms at 20 Hz ($n = 9$).

These results demonstrate that robust spiking can be observed in DB3a and DB4 bipolar cells. The ability to generate spikes will be influenced by the resting potential of the cell, since the fraction of voltage-gated Ca_V and Na_V channels in the inactivated state will increase at depolarized potentials. The resting potential of these bipolar cells *in vivo* is not known; however, in these light-adapted slice preparations, the mean (±SEM) resting potential of DB4 cells, measured under current-clamp, was −59.0 ± 1.2 mV ($n = 8$; range, −64 to −55 mV). Sinusoidal current injections, measured close to a resting potential of −60 mV, generated regenerative voltage responses during the positive phase of the stimulus (Fig. 9*E*). The peak-to-peak amplitude of the linear component of the voltage response was ~9 mV (Fig. 9*E*, cyan), which is within the expected physiological voltage response range. Similar results were found in a further eight DB4 cells. Overall, these results demonstrate that bipolar cells of the magnocellular pathway can produce both spikes and nonlinear depolarizing voltage responses. As expected from the lack of Na_V or Ca_V channels, IMB cells did not display regenerative depolarizations (Fig. 9*F*). FMB cells showed qualitatively similar responses (data not shown).

Bipolar cell spikes are initiated in the AIS

The anatomical data showing the axonal localization of Na_V channels raised the possibility that DB3a and DB4 cells, like other central neurons, might generate action potentials in the AIS that then backpropagate to the soma (for review, see Bender and Trussell, 2012). However, bipolar cells are very small (axonal length, approximately <30 μm), compared with most central neurons, and are generally believed to be isopotential. On the other hand, as noted above, under voltage-clamp we invariably observed action currents near the threshold for Na_V activation, suggesting the presence of unclamped action potentials. Therefore, we constructed a compartmental model of a DB4 cell to determine whether the AIS could be electrically isolated from the soma. The model aimed to recapitulate the currents obtained under voltage-clamp, based on the anatomy of the cells, the localization of the Na_V channels, and the kinetic parameters for $Na_V1.1$ channels. We digitized the morphology of a DB4 cell (Fig. 10*A*) and included a high density of $Na_V1.1$ channels just above the axonal arborization. We calibrated the model by adjusting Na_V and K_V channel densities to reproduce the time course and amplitudes of the average currents activated by voltage steps (Fig. 10*B*; see Materials and Methods). A critical constraint on the model was the observation that action currents first appeared at −55 mV (Fig. 10*C*,*D*), but not at −60 mV. In our voltage-clamp data, action currents occurred with variable amplitudes and latencies at −55 mV in 17 of the 34 DB4 cells (Fig. 10*E*); only 1 DB4 cell produced an action current at −60 mV, while only 4 of 34 cells failed at −50 mV.

Two parameters were critical to reproduce the action currents observed experimentally: the R_i, which determines the electrical coupling between the somatic voltage-clamp and the AIS; and the density of Na_V channels in the AIS (D_{NaV}). Increasing R_i had modest effects on the latency, but strongly suppressed action current amplitude. Conversely, increasing D_{NaV} shortened latency

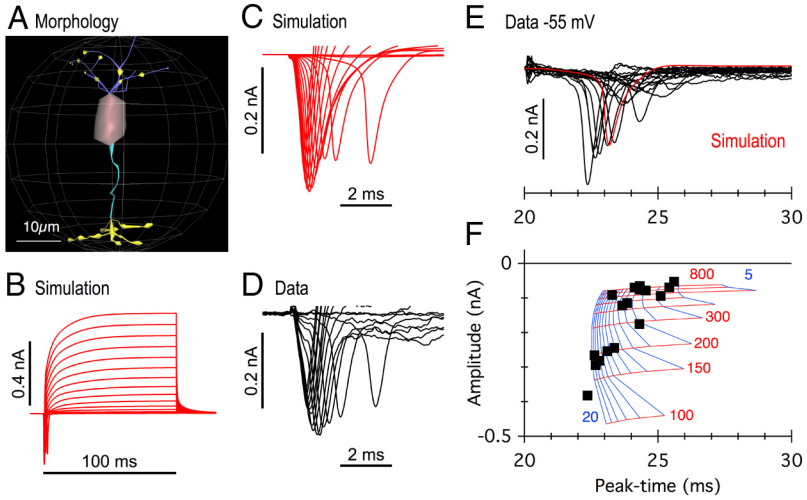

Figure 10. Modeling of sodium spikes in the DB4 cell AIS. ***A***, Morphology of the DB4 cell used for the simulations. ***B***, Simulated currents during depolarizing voltage steps. The voltage protocol is identical to that in Figure 1*I*. ***C***, ***D***, Same as ***B*** on an expanded timescale for the simulation (***C***) and in an example cell (***D***). ***E***, Unclamped action currents first appeared during the step to −55 mV in the model (red) and in 17 of the 34 DB4 cells (black). ***F***, Inward peak amplitude versus time of peak for action currents during steps to −55 mV (solid). The intersections on the lattice show results for simulated action currents at −55 mV, for a range of axonal resistivity (red) and AIS $Na_V1.1$ densities (blue). Blue lines, left to right, represent decrements in density (D_{NaV}) of 1 nS/μm^2. Red lines, bottom to top, represent increments in R_i. Above 300 Ω/cm, R_i was incremented by 100.

with modest effects on amplitude (Fig. 10*F*). The experimental data also showed an increase in action current amplitude for intermediate depolarizations. To reproduce this, the model required a low density of Na_V channels (~15 pS/μm^2) proximal to the AIS. In sum, these results are consistent with an electrically isolated AIS and suggest that AIS Na_V channel density is on the order of 10 nS/μm^2, equivalent to ~600 channels/μm^2 (Vanoye et al., 2006).

Blockade of voltage-gated sodium channels reduces excitatory input to parasol ganglion cells

Next, we examined whether Na_V channels play a role in signaling between bipolar cells and ganglion cells. If DB3a and DB4 cells make input to parasol ganglion cells, and Na_V channels augment synaptic release from the bipolar cells, then TTX should reduce excitatory drive to parasol ganglion cells. To test this hypothesis, we recorded light-evoked synaptic currents (Fig. 11*A*,*B*) in parasol ganglion cells at a range of holding potentials, and calculated the component excitatory and inhibitory inputs (Fig. 11*E–H*). Parasol ganglion cells were readily identified by their large soma size and characteristic transient light responses (Dacey, 1999). The current–voltage relations in parasol ganglion cells were well approximated by the sum of G_{exc} and G_{inh} (Fig. 11*C*,*D*, fitted lines). G_{exc} and G_{inh}, obtained in a representative ON parasol ganglion cell, are shown in Figure 11, *E* and *F*. ON parasol ganglion cells responded to a centered 50% contrast light spot with a transient excitatory input at the onset of the light flash, and larger, transient inhibition at the termination of the flash (Fig. 11*E*,*F*). Bath application of TTX (0.5 μM) significantly reduced the peak excitatory conductance activated at stimulus onset in ON-parasol ganglion cells [peak amplitude ratio, TTX/control, (mean ± SD) 0.58 ± 0.28; $n = 10$ cells; *t* test, $p = 0.00066$; Fig. 11*E*,*I*]. Similarly, TTX suppressed the peak excitatory conductance in OFF parasol ganglion cells [peak amplitude ratio, TTX/control, (mean ± SD) 0.73 ± 0.11; $n = 4$ cells; *t* test, $p = 0.017$; Fig. 11*G*,*I*]. Application of TTX did not alter either the 10–90% rise time or the width at half-peak of G_{exc} (10–90% rise time; ON: control, 21 ± 4 ms; TTX: 25 ± 15 ms; $n = 10$; *t* test, $p = 0.31$; OFF: control, 16 ± 5 ms; TTX: 16 ± 2 ms; $n = 4$; *t* test, $p = 0.93$; half-width is shown in Fig. 11*J*). It is noteworthy that the peak amplitude of the transient inhibition at the termination of the light stimulus was unaffected by TTX (peak amplitude ratio, TTX/control: ON parasol cells: 1.00 ± 0.20; $n = 10$; *t* test, $p = 0.89$; Fig. 11*F*,*I*; OFF parasol cells: 0.83 ± 0.15; $n = 4$; *t* test, $p = 0.11$; Fig. 11*H*,*I*). These results suggest that the amacrine cells that provide inhibitory input to parasol cells, are not driven by bipolar cells that express a high density of Na_V channels.

It is important to note that the recording pipette contained the Na_V channel blocker QX-314, and thus the observed effects of TTX were not due to blockade of TTX-sensitive Na_V channels in ganglion cells (Dhingra et al., 2005). However, TTX could also act at other sites in the retinal network, such as on AII amacrine cells, which generate TTX-sensitive spikelets (Boos et al., 1993; Tamalu and Watanabe, 2007), and make electrical synapses with ON cone bipolar cells (Veruki and Hartveit, 2002), including DB4 and IMB cells (Haverkamp et al., 2003). Thus, to control for an effect of TTX on AII amacrine cells under our recording conditions, we recorded light-evoked responses from ON midget ganglion cells. TTX had no significant effect on the peak amplitude ratio of the light-evoked excitatory conductance in ON midget ganglion cells (TTX/control ratio: 0.95 ± 0.04; $n = 4$; *t* test, $p = 0.15$; Fig. 11*K*,*L*). A similar result was obtained in two OFF midget ganglion cells (peak amplitude ratio, TTX/control: cell 1, 1.02; cell 2, 1.02; data not shown). These results indicate that the effect of TTX on EPSC inputs to parasol ganglion cells most likely arises from suppression of Na_V channels in bipolar cells.

DB4 cells make input to ON-parasol ganglion cells

Since DB4 cells are the only ON bipolar cells that express a high density of Na_V channels (Figs. 1, 5), the effects of TTX suggest a functional connection between DB4 cells and ON parasol ganglion cells. However, apart from their similar stratification depth in the IPL (Boycott and Wässle, 1991), there is no direct anatomical evidence for such connectivity. Since we determined that HCN1 channels could be used as a marker of DB3a/b and DB4 cell axon terminals (Fig. 8), we could use this new marker, together with a synaptic marker, in an effort to anatomically identify synapses between DB4 cells and ON parasol ganglion cells.

Physiologically identified ON parasol ganglion cells were filled with Alexa Fluor 594 during whole-cell recordings (Fig. 12*A*), and retinae were then fixed and labeled for HCN1 and GluR4 ($n = 4$ cells from 4 animals). GluR4 is expressed postsynaptically at the majority of ribbon synapses in the IPL (Jusuf et al., 2006) and thus serves as a marker of excitatory synapses. As expected, ON parasol ganglion cells costratified precisely with the HCN1-positive DB4 boutons (peak HCN1 fluorescence at 60.6 ± 0.9% of IPL; peak ON parasol cell fluorescence at 60.1 ± 0.3%; Fig. 12*B*). Moreover, in all four retinae, HCN1-positive DB4 terminal boutons were seen to wrap around ON parasol ganglion cell dendritic profiles, and the synaptic marker, GluR4, was present at

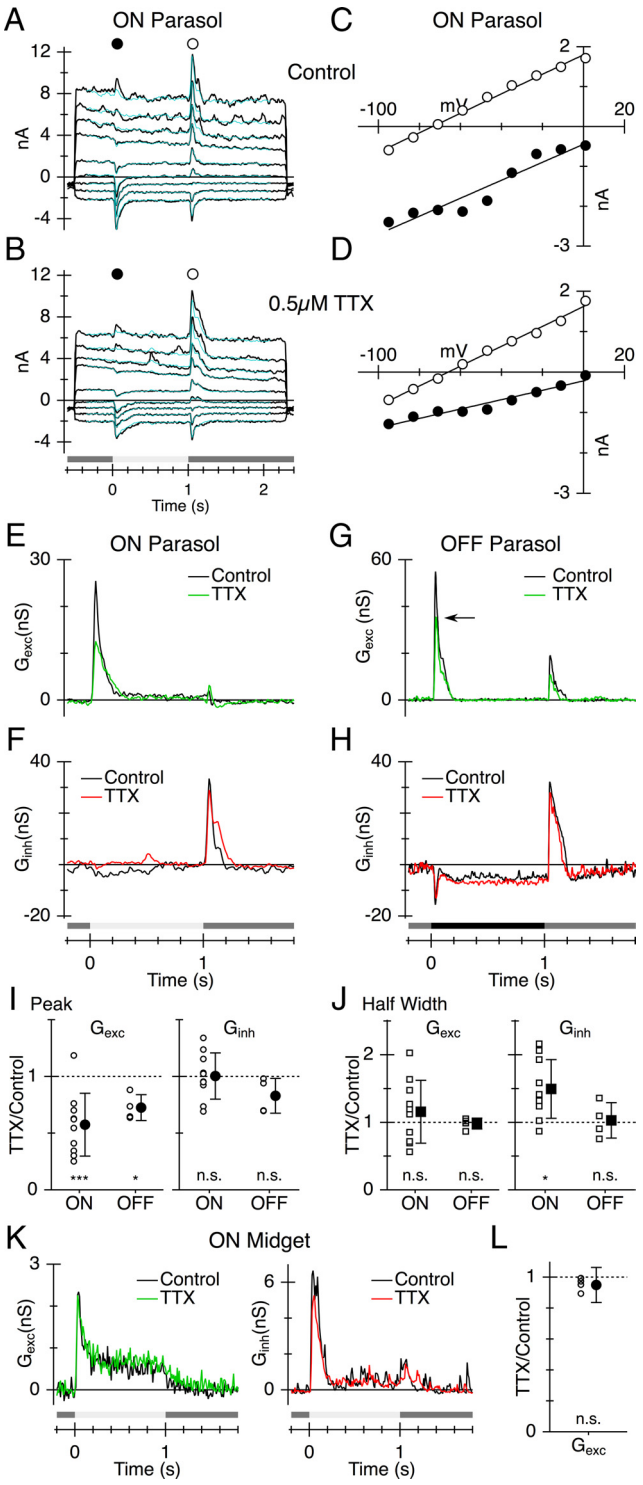

Figure 11. TTX suppresses light-evoked excitatory inputs to parasol ganglion cells. ***A***, ***B***, Light-evoked currents to a 250 μm, 50% contrast spot centered on the receptive field in a representative ON parasol ganglion cell during voltage steps to different holding potentials (−110 to +50 mV in 20 mV increments). Currents are shown in control (***A***) and in the presence of TTX (***B***). Light stimulus timing is indicated beneath the traces in this and subsequent panels. Cyan overlays show the current predicted from G_{exc} and G_{inh} conductances shown in ***E*** and ***F*** (see Materials and Methods). TTX application did not systematically affect the amplitude of the leak currents before the stimulus. ***C***, ***D***, *I–V* relations in control (***C***) and TTX (***D***) measured at the time points shown by the symbols in ***A*** and ***B***. Solid lines show regression fits used to calculate the G_{exc} and G_{inh}. ***E***, ***F***, Linear G_{exc} (***E***) and G_{inh} (***F***) calculated under control conditions (black traces) and in the presence of TTX (colored traces) for a representative ON parasol ganglion cell. ***G***, ***H***, Conductances calculated for a representative OFF parasol ganglion cell under control conditions (black traces) and in the presence of TTX (colored traces). The black arrow shows the peak conductance during TTX application. ***I***, Ratio of peak amplitude (TTX/Control) of G_{exc} and G_{inh} in ON and OFF parasol ganglion cells. Open circles show data from individual cells; filled circles show averages (±1 SD). ***J***, Similar to ***I*** showing half-widths of G_{exc} and G_{inh}. ***K***, Conductances calculated for a representative ON midget ganglion cell under control conditions (black traces) and in the presence of TTX (colored traces). ***L***, Ratio of peak amplitude (TTX/Control) of G_{exc} in four ON midget ganglion cells. Open circles show data from individual cells; filled circles show averages (±1 SD). Paired *t* test, n.s. ($p > 0.05$). *$p < 0.05$, ***$p < 0.001$.

these contact points (Fig. 12*C*), suggesting the presence of a glutamatergic synapse between the two cells. Together, the anatomical and physiological data strongly suggest that DB4 cells provide excitatory input to ON parasol ganglion cells.

Discussion

We have shown that bipolar cells of the magnocellular pathway selectively express $Na_V1.1$ channels in an AIS-like compartment, and that these channels serve to augment excitatory input to ON and OFF parasol ganglion cells. Similarly, $Ca_V3.1$ and HCN1 channels, which are also associated with transient signaling, are expressed in the magnocellular, but not the parvocellular, pathway. Our results also provide evidence for synaptic connectivity between DB4 cells and ON parasol ganglion cells, and identify a new functional bipolar cell type that likely provides input to OFF parasol ganglion cells (DB3b; Fig. 13). Overall, the results support the notion that differences in intrinsic membrane properties, due to selective expression of voltage-gated channels, are an important mechanism for shaping signaling in the magnocellular and parvocellular pathways of the primate retina.

Selective expression of $Na_V1.1$ in transient visual pathways

The results raise the question of whether Na_V currents are a ubiquitous feature of bipolar cells in transient signaling pathways. In the rat retina, an OFF and ON bipolar cell exhibit TTX-sensitive Na_V currents, and, similar to the results here, these cells terminate near the center of the IPL where transient ganglion cells also stratify (Cui and Pan, 2008). In the mouse, an imaging approach demonstrated light-evoked calcium spikes in bipolar cells terminating near the middle of the IPL (Baden et al., 2013a). In ground squirrel retina, light-evoked spikes have been demonstrated in an ON bipolar cell type (cb5b), which costratified with otherwise unidentified ON transient ganglion cells; however, no corresponding OFF bipolar cells were identified (Saszik and DeVries, 2012). Functional evidence for a role of Na_V channels in modifying excitatory input to transient ganglion cells is lacking in these species. In salamander retina, Na_V currents were observed in ON but not OFF bipolar cells, and TTX suppressed excitation of transient, but not sustained, ganglion cells (Ichinose et al., 2005). However, in guinea pig and mouse retinae, the magnitude of excitatory inputs to transient α-ganglion cells were unaffected by TTX (Demb et al., 2001; Tian et al., 2010). Our results show that Na_V channels contribute to signaling in both the ON and OFF transient pathways, but it remains to be confirmed whether this is a primate specialization, or whether Na_V channels contribute to signaling in other vertebrates under some stimulus conditions.

Axon initial segments in magnocellular pathway bipolar cells

We have demonstrated an AIS-like compartment in bipolar cells of the primate magnocellular pathway, which, to our knowledge, is the first evidence for an AIS-like compartment in a bipolar cell of any species. $Na_V1.1$ was present in the AIS of DB3a and DB4 cells, but the other constituents of the AIS differed, with FGF-14

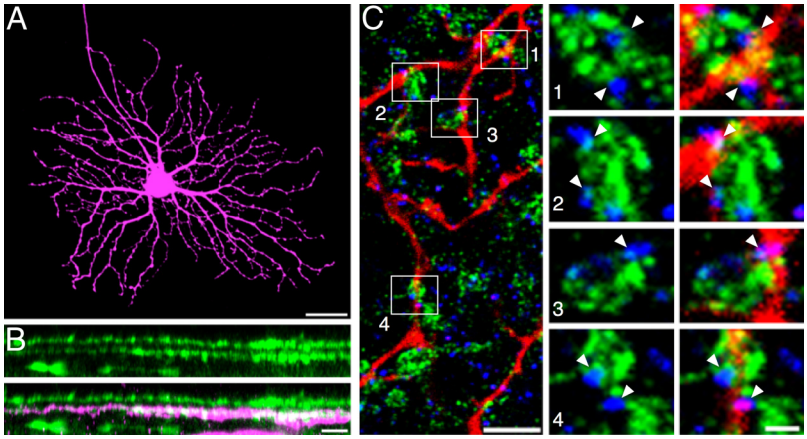

Figure 12. DB4 cells make input to ON parasol ganglion cells. ***A***, Confocal micrograph of a representative ON parasol ganglion cell fill. ***B***, Side view showing costratification of a different ON parasol ganglion cell dendritic arbor (magenta) with the lower band of HCN1-positive boutons (DB4 boutons; green). ***C***, Triple label showing an example of a retinal whole mount in which an ON parasol ganglion cell was filled (red). The retina was then immunostained for HCN1 (green) and the AMPA receptor subunit, GluR4 (blue puncta). Note that GluR4 is located at contact points between the HCN1-positive DB4 boutons and the ON parasol ganglion cell dendritic profiles. Panels numbered 1–4 on the right show regions-of-interest delineated by rectangles in ***C***. Arrowheads indicate sites of putative synaptic connections. Scale bars; ***A***, 20 μm; ***B***, 10 μm; ***C***, 5 μm; ***C***, right panels ***1–4***, 1 μm

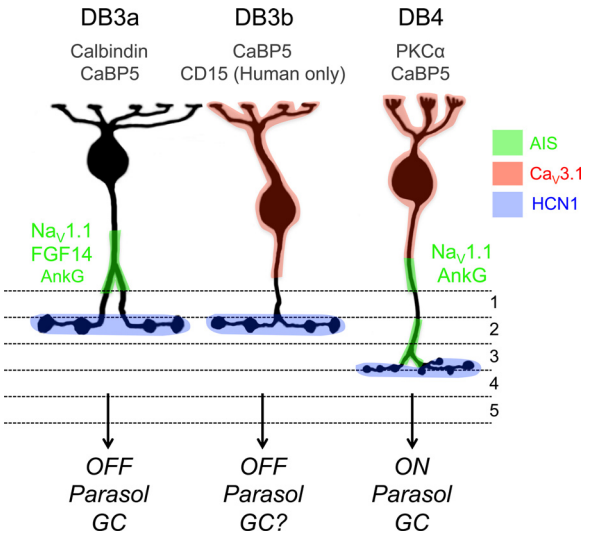

Figure 13. Overview of voltage-gated channels and AIS proteins in bipolar cells of the primate magnocellular pathway. Schematic diagram showing the localization of $Ca_V3.1$, $Na_V1.1$, HCN1 channels, and AIS proteins in bipolar cells that make input to parasol ganglion cells. Immunohistochemical markers of the cell types are indicated in gray text (see also Haverkamp et al., 2003). DB3b cells costratify with DB3a cells and likely provide input to OFF parasol ganglion cells, but direct evidence for synaptic connectivity is yet to be demonstrated.

expressed only in DB3a cells, and higher levels of AnkG expression in DB4 cells. FGF-14 interacts with Na_V α-subunits and can modify channel gating properties and channel density (Lou et al., 2005), which could contribute to differences in spiking properties of DB3a and DB4 cells. Our results contrast with previous studies, which did not detect $Na_V1.1$ in cone bipolar cells of the rodent retina (Van Wart et al., 2005; Mojumder et al., 2007; Wu et al., 2011). Together, these results indicate that the density, distribution and subunit expression of Na_V channels in bipolar cells may differ between primates and other mammals.

Computer simulations based on realistic cell morphology suggest that for reasonable values for the axoplasmic resistivity (Oltedal et al., 2009) the density of Na_V channels in the AIS should be on the order of 10 nS/μm^2 in DB4 cells. Although this is several fold higher than estimates in cortical neurons (Kole and Stuart, 2012), it is important to note that near the measured resting potential of the DB4 cells (approximately −60 mV), a significant fraction of the channels will be inactivated (Kalume et al., 2007). Even so, given the input resistance of these cells (~600 MΩ) only ~30–40 pA of peak Na_V current would be required to depolarize a DB4 cell by ~15–20 mV, enough to contribute to transmitter release. Indeed, DB4 cells showed nonlinear regenerative events in response to relatively small input currents near the resting potential. Moreover, the observed suppression of light-evoked EPSCs in parasol ganglion cells during TTX application suggests that Na_V channels enhance transmitter release from bipolar cells under physiological conditions. Previous work indicates that bipolar cells may be able to switch between spiking and nonspiking signaling modes (Baden et al., 2011; Saszik and DeVries, 2012). Future experiments will be needed to establish whether primate bipolar cells signal via discrete spikes, nonlinear depolarizations, or graded signals depending on the stimulus conditions.

Recent studies demonstrate the capacity for plasticity in the AIS of central neurons (for review, see Grubb et al., 2011). Long-term activity-dependent modulation in AIS length and position have been linked with activation of L- or T-type Ca_V channels, and it is thought that high calcium concentrations might serve as a negative feedback signal for expression of Na_V channels (Sherman and Catterall, 1984; Grubb and Burrone, 2010). Our immunohistochemical results show a relationship among AIS, Ca_V, and Na_V channels that fits well with this hypothesis; in DB4 cells, $Na_V1.1$ channel density varied inversely with $Ca_V3.1$ density. AIS function can also be modulated on short timescales by activating D3 dopamine receptors (Bender et al., 2010), and previous studies indicate that dopamine can modulate bipolar cell Na_V currents (Ichinose and Lukasiewicz, 2007). In this context, it is noteworthy that we saw a reduction in $Na_V1.1$ immunoreactivity in stratum 1 of the IPL, the region where dopaminergic amacrine cells also ramify (Nguyen-Legros et al., 1997). Future studies will examine whether the bipolar cell AIS can be modulated by dopamine or retinal activity.

Potential roles for Na_V, Ca_V, and HCN channels in modifying magnocellular pathway output

As visual contrast increases, the responses of magnocellular, but not parvocellular, cells become more transient (Benardete et al., 1992; Benardete and Kaplan, 1999), a phenomenon known as contrast gain control (Shapley and Victor, 1978). The different Na_V and Ca_V expressions between the two pathways, specifically the lack of Na_V/Ca_V channels in midget bipolar cells, raise the possibility that the intrinsic membrane properties of bipolar cells could contribute to this phenomenon (Beaudoin et al., 2007). The speed and transience of Na_V/Ca_V channel activation in magnocellular pathway bipolar cells could tune the peak sensitivity of these cells, and hence the parasol ganglion cells, to higher temporal frequencies, producing a more bandpass transfer function. The larger bipolar cell depolarizations, produced at higher contrasts,

will be more likely to reach threshold for Na_V/Ca_V channel activation at higher frequencies. Moreover, the larger negative fluctuations in membrane potential associated with high contrast inputs will transiently remove inactivation of the channels and effectively lower the threshold for subsequent regenerative depolarizations. The larger negative fluctuations will also activate HCN1 channels, and thus speed repolarization. Indeed, the probability of a bipolar cell spiking to noisy light stimuli is higher following negative voltage fluctuations (Saszik and DeVries, 2012).

A second, related role of Na_V and Ca_V expression in the magnocellular pathway might be to improve the temporal precision of visual signals (Baden et al., 2011, 2013b). We show that Na_V activation contributes to larger EPSCs in parasol ganglion cells, which will speed depolarization, thus reducing spike-time variability due to membrane voltage fluctuations (Uzzell and Chichilnisky, 2004). An additional consequence of bipolar cell spike initiation in the AIS might be to coordinate transmitter release across terminal boutons within a single cell. The divergence of this synchronized signal could promote the correlated firing observed in neighboring parasol ganglion cells (Trong and Rieke, 2008; Greschner et al., 2011). Indeed, the spatial dimensions of the correlations are similar to that of a bipolar cell receptive field (Trong and Rieke, 2008). Spiking in bipolar cells may also help account for the narrower correlation times seen in parasol ganglion cells compared with noise originating in the cone photoreceptors (Ala-Laurila et al., 2011).

Significance of retinal $Na_V1.1$ expression for neurological disorders

$Na_V1.1$ is expressed in the AIS of GABAergic interneurons, retinal ganglion cells, and spinal cord neurons (for review, see Kole and Stuart, 2012). Our results provide evidence for $Na_V1.1$ in an additional glutamatergic neuron—the retinal bipolar cell. Mutations in the gene encoding $Na_V1.1$ (*SCN1A*) have been implicated in epilepsy and familial hemiplegic migraine (FHM; Catterall et al., 2008), as well as autism spectrum disorders (Han et al., 2012; O'Roak et al., 2012). Interestingly, *SCN1A* mutations have been associated with episodes of "elicited repetitive daily blindness" in patients with co-occurring FHM. This phenomenon, characterized by transient episodes of complete blindness, can be induced monocularly, indicating a retinal origin (Vahedi et al., 2009). The phenotype has been likened to spreading retinal depression, which is thought to be triggered by aberrant neural activity in the inner plexiform layer of the retina (Somjen, 2001). Thus, alterations in bipolar cell $Na_V1.1$ might contribute to the pathogenesis of this condition. Our results suggest that further consideration of the ocular sequelae of human *SCN1A* mutations is warranted, and that attention to magnocellular visual functions could be informative.

References

Ala-Laurila P, Greschner M, Chichilnisky EJ, Rieke F (2011) Cone photoreceptor contributions to noise and correlations in the retinal output. Nat Neurosci 14:1309–1316. CrossRef Medline

Awatramani GB, Slaughter MM (2000) Origin of transient and sustained responses in ganglion cells of the retina. J Neurosci 20:7087–7095. Medline

Baden T, Esposti F, Nikolaev A, Lagnado L (2011) Spikes in retinal bipolar cells phase-lock to visual stimuli with millisecond precision. Curr Biol 21:1859–1869. CrossRef Medline

Baden T, Berens P, Bethge M, Euler T (2013a) Spikes in mammalian bipolar cells support temporal layering of the inner retina. Curr Biol 23:48–52. CrossRef Medline

Baden T, Euler T, Weckström M, Lagnado L (2013b) Spikes and ribbon synapses in early vision. Trends Neurosci 36:480–488. CrossRef Medline

Barrow AJ, Wu SM (2009) Low-conductance HCN1 ion channels augment the frequency response of rod and cone photoreceptors. J Neurosci 29:5841–5853. CrossRef Medline

Beaudoin DL, Borghuis BG, Demb JB (2007) Cellular basis for contrast gain control over the receptive field center of mammalian retinal ganglion cells. J Neurosci 27:2636–2645. CrossRef Medline

Benardete EA, Kaplan E (1999) Dynamics of primate P retinal ganglion cells: responses to chromatic and achromatic stimuli. J Physiol 519:775–790. CrossRef Medline

Benardete EA, Kaplan E, Knight BW (1992) Contrast gain control in the primate retina: P cells are not X-like, some M cells are. Vis Neurosci 8:483–486. CrossRef Medline

Bender KJ, Trussell LO (2009) Axon initial segment Ca2+ channels influence action potential generation and timing. Neuron 61:259–271. CrossRef Medline

Bender KJ, Trussell LO (2012) The physiology of the axon initial segment. Annu Rev Neurosci 35:249–265. CrossRef Medline

Bender KJ, Ford CP, Trussell LO (2010) Dopaminergic modulation of axon initial segment calcium channels regulates action potential initiation. Neuron 68:500–511. CrossRef Medline

Boos R, Schneider H, Wässle H (1993) Voltage- and transmitter-gated currents of all-amacrine cells in a slice preparation of the rat retina. J Neurosci 13:2874–2888. Medline

Boycott BB, Wässle H (1991) Morphological classification of bipolar cells of the primate retina. Eur J Neurosci 3:1069–1088. CrossRef Medline

Buldyrev I, Puthussery T, Taylor WR (2012) Synaptic pathways that shape the excitatory drive in an OFF retinal ganglion cell. J Neurophysiol 107:1795–1807. CrossRef Medline

Calkins DJ, Sterling P (2007) Microcircuitry for two types of achromatic ganglion cell in primate fovea. J Neurosci 27:2646–2653. CrossRef Medline

Calkins DJ, Schein SJ, Tsukamoto Y, Sterling P (1994) M and L cones in macaque fovea connect to midget ganglion cells by different numbers of excitatory synapses. Nature 371:70–72. CrossRef Medline

Catterall WA, Dib-Hajj S, Meisler MH, Pietrobon D (2008) Inherited neuronal ion channelopathies: new windows on complex neurological diseases. J Neurosci 28:11768–11777. CrossRef Medline

Clancy CE, Kass RS (2004) Theoretical investigation of the neuronal Na+ channel SCN1A: abnormal gating and epilepsy. Biophys J 86:2606–2614. CrossRef Medline

Crook JD, Peterson BB, Packer OS, Robinson FR, Gamlin PD, Troy JB, Dacey DM (2008) The smooth monostratified ganglion cell: evidence for spatial diversity in the Y-cell pathway to the lateral geniculate nucleus and superior colliculus in the macaque monkey. J Neurosci 28:12654–12671. CrossRef Medline

Cui J, Pan ZH (2008) Two types of cone bipolar cells express voltage-gated Na+ channels in the rat retina. Vis Neurosci 25:635–645. CrossRef Medline

Dacey D (2004) Origins of perception: retinal ganglion cell diversity and the creation of parallel visual pathways. In: The cognitive neurosciences (Gazzaniga M, ed), pp 281–301. Cambridge, MA: MIT.

Dacey DM (1999) Primate retina: cell types, circuits and color opponency. Prog Retin Eye Res 18:737–763. CrossRef Medline

Demb JB, Zaghloul K, Haarsma L, Sterling P (2001) Bipolar cells contribute to nonlinear spatial summation in the brisk-transient (Y) ganglion cell in mammalian retina. J Neurosci 21:7447–7454. Medline

De Monasterio FM, Gouras P (1975) Functional properties of ganglion cells of the rhesus monkey retina. J Physiol 251:167–195. Medline

DeVries SH (2000) Bipolar cells use kainate and AMPA receptors to filter visual information into separate channels. Neuron 28:847–856. CrossRef Medline

Dhingra NK, Freed MA, Smith RG (2005) Voltage-gated sodium channels improve contrast sensitivity of a retinal ganglion cell. J Neurosci 25:8097–8103. CrossRef Medline

Eggers ED, Lukasiewicz PD (2011) Multiple pathways of inhibition shape bipolar cell responses in the retina. Vis Neurosci 28:95–108. CrossRef Medline

Greschner M, Shlens J, Bakolitsa C, Field GD, Gauthier JL, Jepson LH, Sher A, Litke AM, Chichilnisky EJ (2011) Correlated firing among major ganglion cell types in primate retina. J Physiol 589:75–86. CrossRef Medline

Grubb MS, Burrone J (2010) Activity-dependent relocation of the axon initial segment fine-tunes neuronal excitability. Nature 465:1070–1074. CrossRef Medline

Grubb MS, Shu Y, Kuba H, Rasband MN, Wimmer VC, Bender KJ (2011) Short- and long-term plasticity at the axon initial segment. J Neurosci 31:16049–16055. CrossRef Medline

Grünert U, Martin PR, Wässle H (1994) Immunocytochemical analysis of

bipolar cells in the macaque monkey retina. J Comp Neurol 348:607–627. CrossRef Medline

Han S, Tai C, Westenbroek RE, Yu FH, Cheah CS, Potter GB, Rubenstein JL, Scheuer T, de la Iglesia HO, Catterall WA (2012) Autistic-like behaviour in Scn1a+/− mice and rescue by enhanced GABA-mediated neurotransmission. Nature 489:385–390. CrossRef Medline

Han Y, Jacoby RA, Wu SM (2000) Morphological and electrophysiological properties of dissociated primate retinal cells. Brain Res 875:175–186. CrossRef Medline

Haverkamp S, Haeseleer F, Hendrickson A (2003) A comparison of immunocytochemical markers to identify bipolar cell types in human and monkey retina. Vis Neurosci 20:589–600. CrossRef Medline

Hutcheon B, Yarom Y (2000) Resonance, oscillation and the intrinsic frequency preferences of neurons. Trends Neurosci 23:216–222. CrossRef Medline

Hutcheon B, Miura RM, Puil E (1996) Subthreshold membrane resonance in neocortical neurons. J Neurophysiol 76:683–697. Medline

Ichinose T, Lukasiewicz PD (2007) Ambient light regulates sodium channel activity to dynamically control retinal signaling. J Neurosci 27:4756–4764. CrossRef Medline

Ichinose T, Shields CR, Lukasiewicz PD (2005) Sodium channels in transient retinal bipolar cells enhance visual responses in ganglion cells. J Neurosci 25:1856–1865. CrossRef Medline

Jacoby RA, Marshak DW (2000) Synaptic connections of DB3 diffuse bipolar cell axons in macaque retina. J Comp Neurol 416:19–29. CrossRef Medline

Jacoby RA, Wiechmann AF, Amara SG, Leighton BH, Marshak DW (2000) Diffuse bipolar cells provide input to OFF parasol ganglion cells in the macaque retina. J Comp Neurol 416:6–18. CrossRef Medline

Joo HR, Peterson BB, Haun TJ, Dacey DM (2011) Characterization of a novel large-field cone bipolar cell type in the primate retina: evidence for selective cone connections. Vis Neurosci 28:29–37. CrossRef Medline

Jusuf PR, Martin PR, Grünert U (2006) Synaptic connectivity in the midget-parvocellular pathway of primate central retina. J Comp Neurol 494:260–274. CrossRef Medline

Kalume F, Yu FH, Westenbroek RE, Scheuer T, Catterall WA (2007) Reduced sodium current in Purkinje neurons from $Na_V1.1$ mutant mice: implications for ataxia in severe myoclonic epilepsy in infancy. J Neurosci 27:11065–11074. CrossRef Medline

Kolb H, Dekorver L (1991) Midget ganglion cells of the parafovea of the human retina: a study by electron microscopy and serial section reconstructions. J Comp Neurol 303:617–636. CrossRef Medline

Kole MH, Stuart GJ (2012) Signal processing in the axon initial segment. Neuron 73:235–247. CrossRef Medline

Kordeli E, Lambert S, Bennett V (1995) AnkyrinG. A new ankyrin gene with neural-specific isoforms localized at the axonal initial segment and node of Ranvier. J Biol Chem 270:2352–2359. CrossRef Medline

Lee BB, Martin PR, Grünert U (2010) Retinal connectivity and primate vision. Prog Retin Eye Res 29:622–639. CrossRef Medline

Lou JY, Laezza F, Gerber BR, Xiao M, Yamada KA, Hartmann H, Craig AM, Nerbonne JM, Ornitz DM (2005) Fibroblast growth factor 14 is an intracellular modulator of voltage-gated sodium channels. J Physiol 569:179–193. CrossRef Medline

Ma YP, Cui J, Hu HJ, Pan ZH (2003) Mammalian retinal bipolar cells express inwardly rectifying K+ currents (IKir) with a different distribution than that of Ih. J Neurophysiol 90:3479–3489. CrossRef Medline

Masland RH (2012) The neuronal organization of the retina. Neuron 76:266–280. CrossRef Medline

Mojumder DK, Frishman LJ, Otteson DC, Sherry DM (2007) Voltage-gated sodium channel alpha-subunits Na(v)1.1, Na(v)1.2, and Na(v)1.6 in the distal mammalian retina. Mol Vis 13:2163–2182. Medline

Müller F, Scholten A, Ivanova E, Haverkamp S, Kremmer E, Kaupp UB (2003) HCN channels are expressed differentially in retinal bipolar cells and concentrated at synaptic terminals. Eur J Neurosci 17:2084–2096. CrossRef Medline

Nguyen-Legros J, Simon A, Caillé I, Bloch B (1997) Immunocytochemical localization of dopamine D1 receptors in the retina of mammals. Vis Neurosci 14:545–551. CrossRef Medline

Oltedal L, Veruki ML, Hartveit E (2009) Passive membrane properties and electrotonic signal processing in retinal rod bipolar cells. J Physiol 587:829–849. CrossRef Medline

O'Roak BJ, Vives L, Girirajan S, Karakoc E, Krumm N, Coe BP, Levy R, Ko A, Lee C, Smith JD, Turner EH, Stanaway IB, Vernot B, Malig M, Baker C, Reilly B, Akey JM, Borenstein E, Rieder MJ, Nickerson DA, et al (2012) Sporadic autism exomes reveal a highly interconnected protein network of de novo mutations. Nature 485:246–250. CrossRef Medline

Pan ZH, Hu HJ, Perring P, Andrade R (2001) T-type Ca(2+) channels mediate neurotransmitter release in retinal bipolar cells. Neuron 32:89–98. CrossRef Medline

Perez-Reyes E (2003) Molecular physiology of low-voltage-activated t-type calcium channels. Physiol Rev 83:117–161. CrossRef Medline

Perry VH, Oehler R, Cowey A (1984) Retinal ganglion cells that project to the dorsal lateral geniculate nucleus in the macaque monkey. Neuroscience 12:1101–1123. CrossRef Medline

Polyak SL (1941) The retina. Chicago: University of Chicago.

Saszik S, DeVries SH (2012) A mammalian retinal bipolar cell uses both graded changes in membrane voltage and all-or-nothing Na^+ spikes to encode light. J Neurosci 32:297–307. CrossRef Medline

Schachter MJ, Oesch N, Smith RG, Taylor WR (2010) Dendritic spikes amplify the synaptic signal to enhance detection of motion in a simulation of the direction-selective ganglion cell. PLoS Comput Biol 6:e1000899. CrossRef Medline

Shapley RM, Victor JD (1978) The effect of contrast on the transfer properties of cat retinal ganglion cells. J Physiol 285:275–298. Medline

Sherman SJ, Catterall WA (1984) Electrical activity and cytosolic calcium regulate levels of tetrodotoxin-sensitive sodium channels in cultured rat muscle cells. Proc Natl Acad Sci U S A 81:262–266. CrossRef Medline

Smith RG (1992) NeuronC: a computational language for investigating functional architecture of neural circuits. J Neurosci Methods 43:83–108. CrossRef Medline

Somjen GG (2001) Mechanisms of spreading depression and hypoxic spreading depression-like depolarization. Physiol Rev 81:1065–1096. Medline

Tamalu F, Watanabe S (2007) Glutamatergic input is coded by spike frequency at the soma and proximal dendrite of AII amacrine cells in the mouse retina. Eur J Neurosci 25:3243–3252. CrossRef Medline

Tian M, Jarsky T, Murphy GJ, Rieke F, Singer JH (2010) Voltage-gated Na channels in AII amacrine cells accelerate scotopic light responses mediated by the rod bipolar cell pathway. J Neurosci 30:4650–4659. CrossRef Medline

Trong PK, Rieke F (2008) Origin of correlated activity between parasol retinal ganglion cells. Nat Neurosci 11:1343–1351. CrossRef Medline

Uzzell VJ, Chichilnisky EJ (2004) Precision of spike trains in primate retinal ganglion cells. J Neurophysiol 92:780–789. CrossRef Medline

Vahedi K, Depienne C, Le Fort D, Riant F, Chaine P, Trouillard O, Gaudric A, Morris MA, Leguern E, Tournier-Lasserve E, Bousser MG (2009) Elicited repetitive daily blindness: a new phenotype associated with hemiplegic migraine and SCN1A mutations. Neurology 72:1178–1183. CrossRef Medline

Van Wart A, Boiko T, Trimmer JS, Matthews G (2005) Novel clustering of sodium channel Na(v)1.1 with ankyrin-G and neurofascin at discrete sites in the inner plexiform layer of the retina. Mol Cell Neurosci 28:661–673. CrossRef Medline

Vanoye CG, Lossin C, Rhodes TH, George AL Jr (2006) Single-channel properties of human NaV1.1 and mechanism of channel dysfunction in SCN1A-associated epilepsy. J Gen Physiol 127:1–14. CrossRef Medline

Venkataramani S, Taylor WR (2010) Orientation selectivity in rabbit retinal ganglion cells is mediated by presynaptic inhibition. J Neurosci 30:15664–15676. CrossRef Medline

Veruki ML, Hartveit E (2002) Electrical synapses mediate signal transmission in the rod pathway of the mammalian retina. J Neurosci 22:10558–10566. Medline

Watanabe M, Rodieck RW (1989) Parasol and midget ganglion cells of the primate retina. J Comp Neurol 289:434–454. CrossRef Medline

Wu C, Ivanova E, Cui J, Lu Q, Pan ZH (2011) Action potential generation at an axon initial segment-like process in the axonless retinal AII amacrine cell. J Neurosci 31:14654–14659. CrossRef Medline

Zhou D, Lambert S, Malen PL, Carpenter S, Boland LM, Bennett V (1998) AnkyrinG is required for clustering of voltage-gated Na channels at axon initial segments and for normal action potential firing. J Cell Biol 143:1295–1304. CrossRef Medline